Mineralogical Magazine (2024), **88**, 682–697
doi:10.1180/mgm.2024.70

CAMBRIDGE UNIVERSITY PRESS

Article

Comparative thermal and compressional behaviour of natural xenotime-(Y), chernovite-(Y) and monazite-(Ce)

Mineralogy, petrology and geochemistry of pegmatites: Alessandro Guastoni memorial issue

Francesco Pagliaro[1], Davide Comboni[1,2], Tommaso Battiston[1], Hannes Krüger[3], Clivia Hejny[3], Volker Kahlenberg[3], Lara Gigli[4], Konstantin Glazyrin[5], Hanns-Peter Liermann[5], Gaston Garbarino[2], G. Diego Gatta[1] and Paolo Lotti[1]

[1]Dipartimento di Scienze della Terra, Università degli Studi di Milano, Via Botticelli 23, 20133 Milano, Italy; [2]European Synchrotron Radiation Facility, 71 Avenue des Martyrs, CS 40220, 38043 Grenoble Cedex 9, France; [3]Institut für Mineralogie und Petrographie, Universität Innsbruck, Innrain 52, 6020 Innsbruck, Austria; [4]Elettra Sincrotrone Trieste S.c.P.A., Strada Statale 14 – km 163.5, 34149 Basovizza, Trieste, Italy and [5]Deutsches Elektronen-Synchrotron DESY, Notkestrasse 85, 22607 Hamburg, Germany

Abstract

ATO_4 compounds are a class of oxides which includes the rare earth element (REE) bearing phosphates and arsenates, $REEPO_4$ and $REEAsO_4$. In this study, we have investigated the isothermal high-pressure and the isobaric high-temperature behaviour of natural samples of xenotime-(Y) (ideally YPO_4), chernovite-(Y) ($YAsO_4$) and monazite-(Ce) ($CePO_4$) from the hydrothermal veins cropping out at Mt. Cervandone in the Western Italian Alps. Experimental data based on *in situ* X-ray diffraction (both single-crystal and powder techniques with conventional or synchrotron radiation) have allowed us to fit the unit-cell volumes and axial thermal and compressional evolution and provide a suite of refined thermo-elastic parameters. A comprehensive analysis of the role played by the crystal chemistry on the thermo-elastic response of these minerals is discussed, along with the description of the main crystal-structural deformation mechanisms for both the zircon (xenotime and chernovite) and monazite (monazite) structural types. Pressure-induced phase transitions of xenotime-(Y) and chernovite-(Y) are discussed and compared with previous literature data, whereas a change in the compressional behaviour of monazite-(Ce) at ∼18 GPa, involving an increase in the coordination number of the REE-hosting *A* site, is presented and discussed.

Keywords: xenotime; monazite; chernovite; ATO_4; pressure; temperature; phase transition; X-ray diffraction

(Received 15 July 2024; accepted 9 September 2024; Accepted Manuscript published online: 12 November 2024)

Introduction

The general formula *ATO*4 is commonly used in the literature to define ternary inorganic oxides (Vorres, 1962), where *A* and *T* represent two cations that can be combined with oxygen (and occasionally with other anions) into several structural types, including, but not limited to, scheelite, zircon, monazite, fergusonite, baryte, quartz, cristobalite, wolframite and rutile (Fukunaga and Yamaoka, 1979). In the context of the present study, the *A* site is occupied by a rare earth element (REE: lanthanides and Y), Ca, U and Th, whereas *T* stands for tetrahedrally-coordinated cations (As and P). In regard to the structural types, this manuscript focuses almost exclusively on the zircon and monazite structures, as demonstrated by the four minerals which are subject of this and two previous works (Pagliaro *et al.*, 2022a, 2022b): chernovite-(Y) [nominally $YAsO_4$], xenotime-(Y) [nominally YPO_4], gasparite-(Ce) [nominally $CeAsO_4$] and monazite-(Ce) [nominally $CePO_4$]. The crystal structure of these minerals has been the subject of a large number of studies and reviews (*e.g.* Mooney, 1948; Ni *et al.*, 1995; Boatner, 2002; Finch and Hanchar, 2003 Kolitsch and Holtstam, 2004; Clavier *et al.*, 2011) and an overview of the monoclinic monazite-type structure and of the tetragonal zircon-type (also known, but occasionally reported as 'xenotime-type') is discussed in the next section.

As reported by several authors (Fukunaga and Yamaoka, 1979; Ushakov *et al.*, 2001; Boatner, 2002; Kolitsch and Holtsam, 2004),

Corresponding author: Paolo Lotti; Email: paolo.lotti@unimi.it
Guest Editor: Fabrizio Nestola
Dedicated to the memory of Dr. Alessandro Guastoni
Cite this article: Pagliaro F. *et al.* (2024). Comparative thermal and compressional behaviour of natural xenotime-(Y), chernovite-(Y) and monazite-(Ce). *Mineralogical Magazine* **88**, 682–697. https://doi.org/10.1180/mgm.2024.70

whether the monazite or the zircon-type structure is stable (within ATO_4 phosphates and arsenates) depends on different factors. Among others, the atomic radii of either the *A* or *T* sites play a dominant role. In general, a large sized *A* cation promotes the crystallisation of the monazite structural type over the zircon one; on the other hand, the larger the *T*-site cation, the more stable is the zircon structure across the REE series. Within the REE-bearing phosphates, light REE ranging from La to Eu, with larger ionic radii than heavy REE, are hosted preferentially by the monazite-type structure, whereas heavy-REE, from Tb to Lu, including Y and Sc, fit best into the zircon-type structure (Mooney, 1948; Ni *et al.*, 1995; Boatner, 2002; Kolitsch and Holtstam, 2004; Clavier *et al.*, 2011). A similar behaviour has been reported for the $REEAsO_4$ series, although the threshold among the two structures is shifted to smaller *Z* numbers in the lanthanoid series: the monazite-type structure preferentially hosts REE from La to Nd, whereas the REE from Sm to Lu (as well as Y and Sc) are hosted by the tetragonal zircon-type crystal structure (*e.g.* Ushakov *et al.*, 2001; Boatner, 2002).

The REE-bearing phosphates are common accessory minerals in hydrothermal alteration of granitoid rocks that can control the partitioning of REE, as well as uranium and thorium, as they tend to incorporate these elements into their crystal structures (Rapp and Watson, 1986). In addition, due to their much lower tendency to incorporate Pb, they have found a significant use in geochronological applications (Harrison *et al.*, 2002). Due to their peculiar physical, chemical and optical properties (such as low solubility in water fluids), REE phosphates are used, or have been proposed, in several technological applications, *e.g.* to produce phosphors (de Sousa Filho and Serra, 2009), ceramic coatings (Morgan *et al.*, 1995; Davis *et al.*, 1998), and materials for the safe storage of actinides originating from radioactive waste (Oelkers and Montel, 2008; Orlova and Ojovan, 2019). Consequently, there has been significant interest in studying the behaviour of REE phosphate minerals and their synthetic counterparts under varying pressure and temperature conditions.

Recent reviews have been published by Errandonea (2017) and Strzelecki *et al.* (2024) for monazite- and zircon-type structures, respectively. Tables S1 and S2 (supplementary material, see below) provide a comprehensive list of the thermo-elastic parameters published in the literature for several $REETO_4$ compounds, along with the related bibliographic references. Concerning the response of $REETO_4$ compounds to high pressure (hereafter H*P*), as a general rule it has been postulated that, for a given structural type, the bulk modulus shifts towards lower values as the atomic radius of the *A* and *T* sites increases, which has been highlighted by several authors and corroborated by both theoretical (Zhang *et al.*, 2008; Li *et al.*, 2009) and experimental studies (Zhang *et al.*, 2008; Lacomba-Perales *et al.*, 2010; Errandonea *et al.*, 2011). Regarding the thermal behaviour, there is general agreement on the thermal expansion coefficient of $REETO_4$, which shows a clear compositional trend: the thermal expansivity increases along with the ionic radii of the *A* cation, while it reduces if the radius of the *T* site increases (Subbarao *et al.*, 1990; Perrière *et al.*, 2007; Zhang *et al.*, 2008; Li *et al.*, 2009). Unfortunately, the published values of both the compressibility and thermal expansivity of the $REETO_4$ studied are not always internally consistent (see Tables S1 and S2), showing a certain degree of scattering, even for the same compound. In the case of thermal studies, the use of different thermal equations of state further complicates a comparative analysis. Therefore, in this study, we used the linear thermal expansion coefficient, which is commonly used in the literature, although it is not the most accurate model of the thermal elastic response (along with thermal equations of state commonly used in Earth Sciences).

The relative ratio of the *A* and *T* ionic radii not only affects the structure types adopted by a given compound at ambient conditions, but also its pressure stability field and the structural type of the high-pressure polymorphs. Such a relationship is well described by the so-called 'Bastide diagram' (Bastide, 1987), for which one of the most recent graphical representations is reported in Lopez-Solano *et al.* (2010) (Fig. 1, modified). The zircon-type compounds, xenotime-(Y) and chernovite-(Y) in this study, may transform at high-pressure into monazite-type or scheelite-type polymorphs. Whether a zircon → scheelite or a zircon → monazite → scheelite transformation occurs depends on the reciprocal relations among the ionic radii of the three atoms involved. A large *T* cation promotes a zircon-to-scheelite phase transition, whereas a small *T* cation favours an intermediate monazite-type polymorph. For the *A*-site cation, the larger it is, the more likely it is that a monazite polymorph will form over the scheelite one, 'shifting' the stability field to higher pressures. All the studied zircon-type ATO_4 silicates show a zircon-to-scheelite phase transition, with high-pressure Raman and Density Functional Theory calculations suggesting the occurrence of a high-pressure lower symmetry polymorph preserving the zircon structural configuration before the reconstructive phase transition to reidite (Stangarone *et al.*, 2019). The zircon-to-scheelite phase transition has been described for $YAsO_4$ (∼8 GPa) and $YCrO_4$ (∼4.2 GPa) (Errandonea *et al.*, 2011), as well as YVO_4 (above ∼7.5 GPa) (Jayaraman *et al.*, 1987; Wang *et al.*, 2004; Manjón *et al.*, 2010). A comprehensive description of the zircon-to-monazite phase transition in phosphates, including YPO_4 (xenotime) is reported in Hay *et al.* (2013). The relations between monazite and its H*P*-polymorphs again depend upon the reciprocal relations among the *A, T* and oxygen ionic radii. The monazite-to-post-baryte phase transition (space group $P2_12_12_1$) has been described for $REEPO_4$ and $REEVO_4$ at increasing pressures with decreasing REE atomic radius (Lacomba-Perales *et al.*, 2010; Ruiz-Fuertes *et al.*, 2016; Errandonea, 2017). On the other hand, monazite-type $LaVO_4$, $PrVO_4$ and $NdVO_4$, under compression, undergo a phase transition to a monoclinic $BaWO_4$-II-type structure (Errandonea *et al.*, 2016; Panchal *et al.*, 2017; Marqueño *et al.*, 2021). Eventually, the monazite-to-scheelite transition has been described for the high-pressure polymorphs of YPO_4 and several other REE-free compounds, as $SrCrO_4$ and $CaSeO_4$ (Crichton *et al.*, 2012; Gleissner *et al.*, 2016).

This study, following the research conducted by Pagliaro *et al.* (2022a, 2022b), which includes a detailed crystal chemistry description, focuses on the high-pressure and temperature behaviour of four $REETO_4$ mineralogical species from the same locality (Mt. Cervandone, Piedmont, Italy).

Based on experimental single-crystal or powder X-ray diffraction data collected *in situ* (high-*P* or high-*T*) at synchrotron beamlines or in conventional diffraction laboratories, a comparative analysis of the elastic behaviour and structural deformation mechanisms as a function of the crystal chemistry and structure type has been performed. The adoption of up-to-date experimental techniques and crystallographic methods has allowed us to describe a *P*-induced structural re-arrangement peculiar of the monazite structure type, previously reported by Pagliaro *et al.* (2022b) for gasparite-(Ce) and here confirmed also for monazite-(Ce). Such an intermediate structural configuration, implying an increase in the number of oxygen atoms bonded to the *A* site (from 9 to 10), before the occurrence of the phase transition to the post-baryte-type

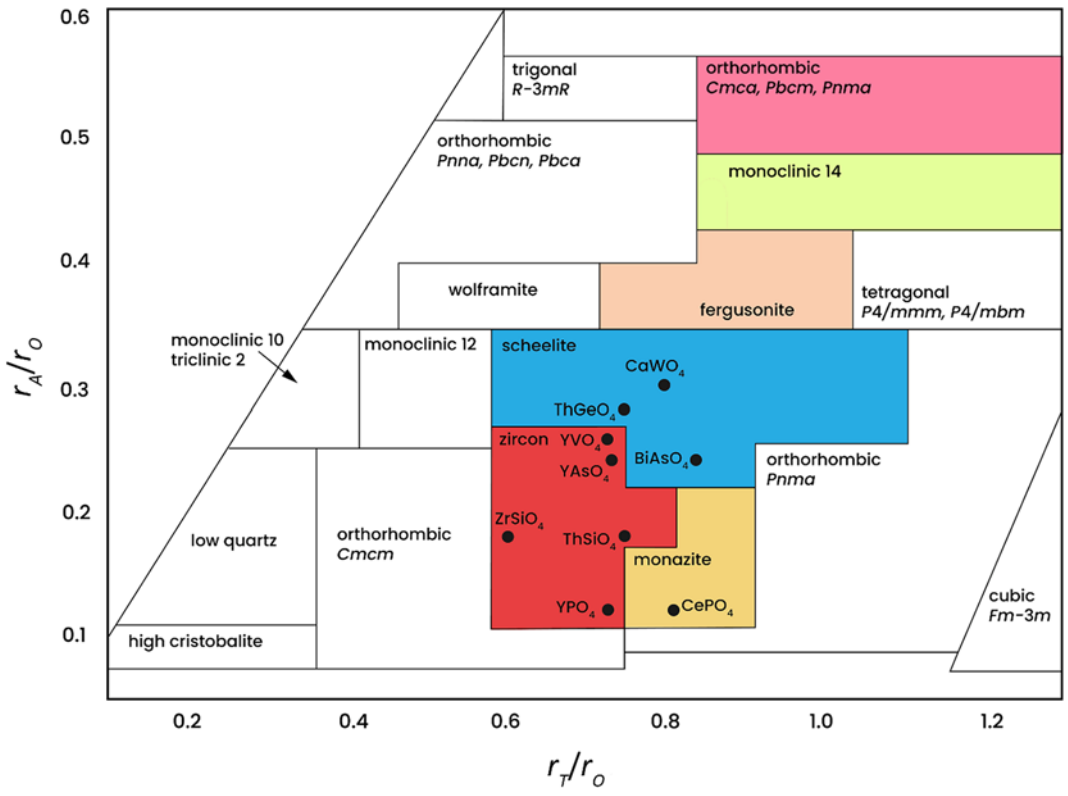

Figure 1. The so-called 'Bastide diagram' showing the relationships among structural types as a function of the atomic radii of cations at the *A* site (r_A), *T* site (r_T) and oxygen (r_O), within the ATO_4 family. The fields corresponding to the $SrUO_4$ and $BaWO_4$-II structures are labelled as orthorhombic (*Cmca, Pbcm, Pnma*) and monoclinic 14, respectively (2, 10, 12, 14 refer to the space group numbers). The post-baryte field is not reported (modified after López-Solano *et al.*, 2010).

polymorph at higher pressures, has not been reported in earlier literature for monazite-type phosphates.

Crystal structure description

Zircon-type crystal structure

The first studies concerning the crystal structure of zircon date back to the early 20th century and were carried out independently by Vegard (1916, 1926), Binks (1926), Hassel (1926) and Wyckoff and Hendricks (1928), in the framework of the pioneering works about the silicate's structure determination, later gathered by Bragg (1929) in his *Atomic Arrangement in Silicates*. After the first studies on zircon, its structural type has been described in several REE-bearing compounds, including xenotime-(Y) (Vegard, 1927) and the synthetic counterpart of chernovite-(Y), $YAsO_4$ (Strada and Schwendimann, 1934).

The zircon-type structure is characterised by a tetragonal *I*-centred lattice (space group $I4_1/amd$). The tetragonal zircon-type structure is constructed by infinite chains of polyhedra, developed along the [001] direction (Fig. 2a and 2d), as the result of the connection, along the polyhedral edges, between the eightfold coordinated *A*-site dodecahedron (AO_8 or $REEO_8$) and the TO_4 tetrahedra (Fig. 2c). The AO_8 polyhedron displays two independent *A*–O atomic distances (Fig. 2c), whereas the TO_4 is an undistorted tetrahedron defined by a single *T*–O bond distance. Each chain is in contact with four others on the (001) plane, through connecting edges along an AO_8 unit and the surrounding four (Fig. 2b). The atomic coordinates of the *A*- and *T*-sites are placed in special, fixed positions, both characterised by a *2m* point symmetry. The oxygen atom is also at a special position (*m*), being its *y* and *z* coordinates the sole refinable parameters.

Monazite-type crystal structure

Parrish (1939), within the first crystallographic studies on monazites, identified its correct space group as $P2_1/n$. The first description of the monazite-type structure has been reported by Mooney (1948), who investigated the La, Ce, Pr and Nd phosphates as part of the Manhattan project and described the REE atomic site in eightfold coordination. The crystal structure of monazite with the REE site in ninefold coordination has been proposed by Ueda (1953, 1967), but with non-reliable average P–O bond lengths of ~1.6 Å. The structure was later described correctly by Beall *et al.* (1981), Mullica *et al.* (1984) and Ni *et al.* (1995), whereas an exhaustive review of the monazite-structure type has been carried out by Boatner (2002) and then by Clavier *et al.* (2011). The monazite-type structure can be described as made by infinite chains running along the [001] direction (*c*-axis), comprising the alternation of the REE-coordination polyhedra and the *T*-hosting tetrahedra (Fig. 3).

The REE-polyhedron coordination environment has nine corners (oxygen ligands, $REEO_9$, Fig. 3c). According to Mullica *et al.* (1984), the $REEO_9$ polyhedron can be described as an equatorial pentagon (sharing vertices with five TO_4 tetrahedra of five adjacent chains in correspondence of the $O1_b$, $O2_b$, $O2_c$, $O3_b$ and $O4_b$ oxygens), interpenetrated by a tetrahedron (made by the $O1_a$, $O2_a$, $O3_a$ and $O4_a$ oxygen atoms, see Fig. 3c), which is along the [001] direction in contact with two subsequent TO_4 tetrahedra, leading to

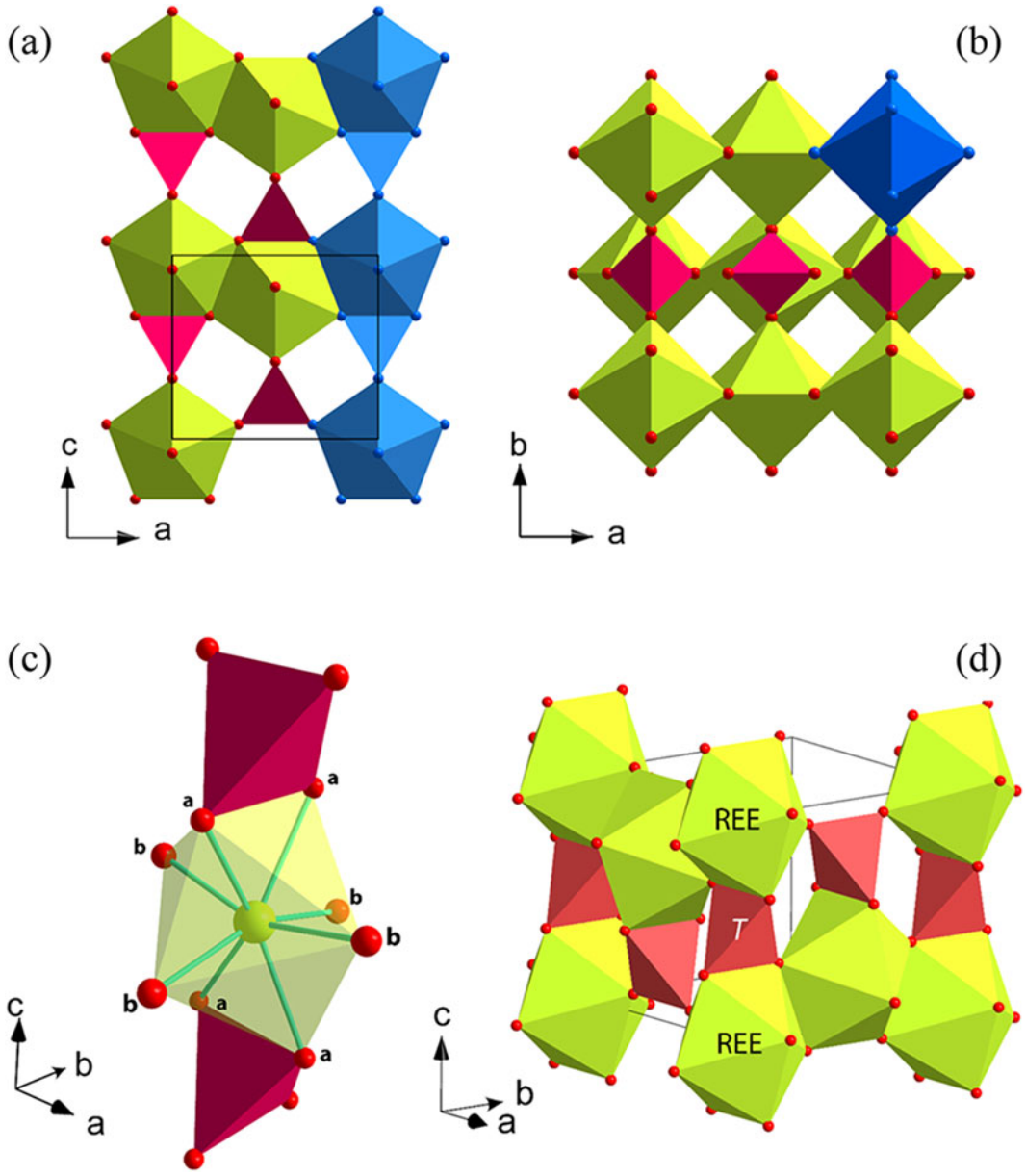

Figure 2. Crystal structure of the zircon-type materials viewed (a) along the [010] and (b) [001] directions and showing (c) the chains running along the **c** directions and the bond distances configuration among the AO_8 polyhedron and (d) a side view of the overall crystal structure. Structure drawings have been made using the software *Vesta3* (Momma and Izumi, 2011).

the formation of the infinite chain units (Fig. 3a,b). The REE–$O2_a$ bond length is significantly longer than the other REE–O bonds, contributing to a significant distortion of the $REEO_9$ polyhedron (Beall *et al.*, 1981; Ni *et al.*, 1995; Clavier *et al.*, 2011), which can be considered as 8+1 coordinated.

Samples and experimental methods

The mineral samples of monazite-(Ce), xenotime-(Y) and chernovite-(Y), investigated in this study, originate from the same locality at Mt. Cervandone, Piedmont, Italian western Alps, where they are found as accessory phases in alpine-type fissures within hydrothermal quartz veins (Graeser and Albertini, 1995) that cross-cut pegmatitic dykes (Guastoni *et al.*, 2006). The latter, intruded in leucocratic gneisses, are enriched in REE and have a strong NYF (Niobium-Yttrium-Fluorine enrichment) signature (Černý, 1991a, 1991b; Černý and Ercit, 2005). An overview of the geological background of the source rocks is described in Pagliaro *et al.* (2022a), along with a detailed chemical analysis of the samples of this study by means of an electron microprobe operating in WDS mode. The experimental chemical formulas of the investigated minerals are summarised in Table 1.

In situ high-pressure experiments

In situ high-pressure single-crystal synchrotron X-ray diffraction experiments have been conducted on chernovite-(Y), xenotime-(Y) and monazite-(Ce) at the P02.2 beamline (PETRA-III synchrotron at DESY, Hamburg, Germany) and ID15B beamline (European Synchrotron Radiation Facility, Grenoble, France)

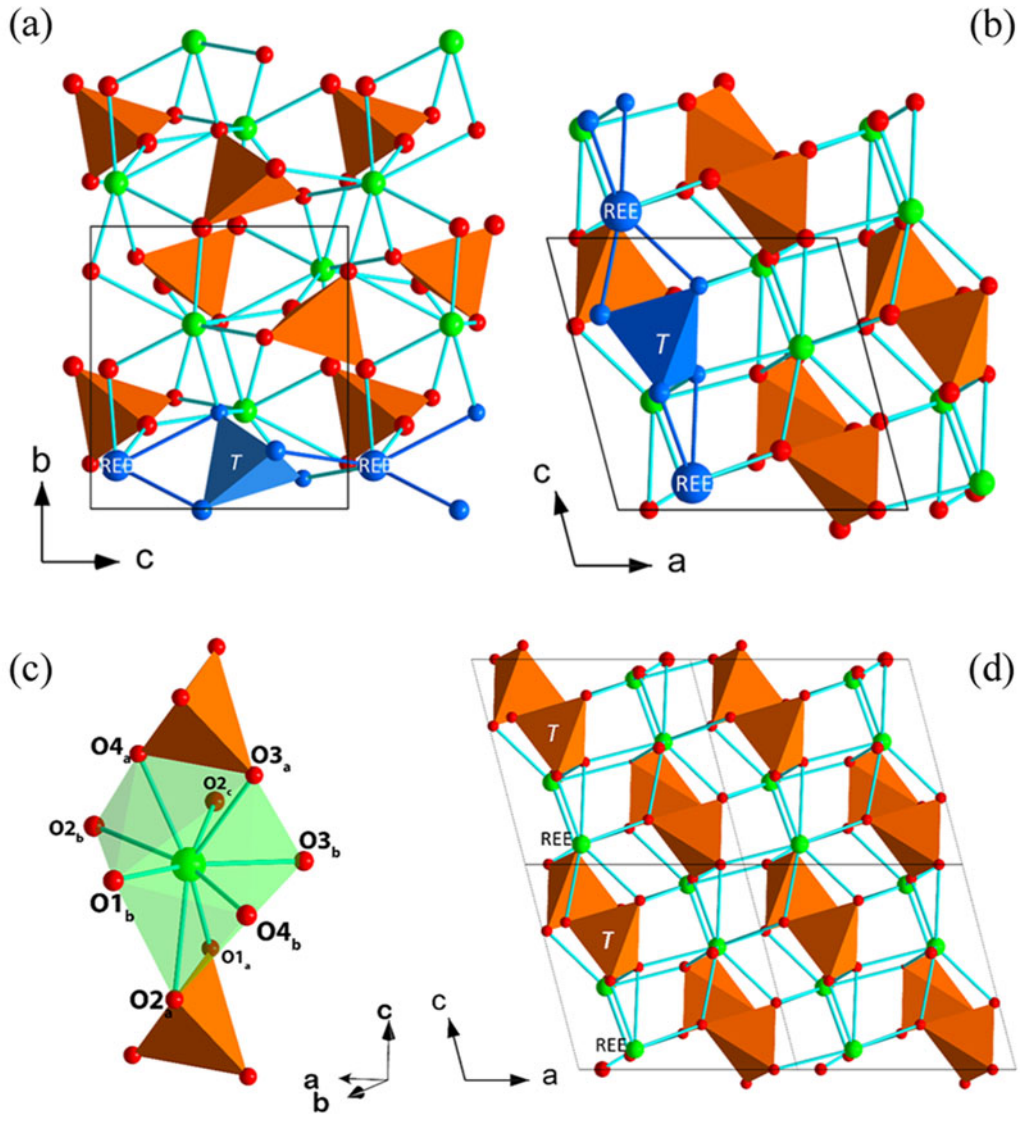

Figure 3. Crystal structure of monazite, viewed along (a) the [100] and (b) [010] directions; a chain-like unit is highlighted in blue; (c) coordination polyhedron of the REE-bearing *A* site, with 9 independent *A*–O bonds; and (d) general view of the monazite structure. Structure drawings have been made using the software *Vesta3* (Momma and Izumi, 2011).

using different classes of *P*-transmitting fluids as shown in Table 2. For all the experiments, the crystals were loaded in membrane-driven diamond anvil cells (DAC), equipped with Boehler-Almax designed diamonds/seats. Metallic foils (steel or rhenium) were pre-indented to ca. 40–70 μm and then drilled by spark-erosion to obtain *P*-chambers. Ruby spheres were employed as pressure calibrants (pressure uncertainty ±0.05 GPa; Mao *et al.*, 1986; Chervin *et al.*, 2001). All data collections were based on a ω-rotation with 0.5° per step and 0.5 s (monazite and chernovite) or 1 s (xenotime) of exposure time per frame. At ID15B, X-ray diffraction (XRD) data were collected using an Eiger2 9M CdTe detector positioned at 179 mm from the sample with a monochromatic 30.2 keV ($\lambda = 0.4099$ Å) beam, whereas XRD patterns at P02.2 were collected on a Perkin Elmer XRD1621 detector at 373 mm from the sample and a monochromatic incident beam with $E = 42.67$ keV ($\lambda = 0.2906$ Å). Further details on the beamlines setups are presented in Merlini and Hanfland (2013) and Poreba *et al.* (2022) for ID15B and Rothkirch *et al.* (2013), Liermann *et al.* (2015) and Bykova *et al.* (2019) for P02.2. Indexing of the X-ray diffraction peaks, unit-cell refinements and intensity data reductions were performed using the *CrysAlisPro* package (Rigaku Oxford Diffraction, 2020). Absorption effects, due to the DAC components, were corrected using the semi-empirical ABSPACK routine, implemented in *CrysAlisPro*.

Based on the experimental intensity single-crystal XRD data, the structure refinements were performed using the *Jana2020* software (Petříček *et al.*, 2023), starting from the structural models reported by Pagliaro *et al.* (2022a) for the mineral samples from the same locality. The site occupancy factors of the *A* (lanthanide-bearing) and tetrahedral sites were fixed according to the average chemical composition obtained from EPMA-WDS analysis (Table 1), disregarding the elements with a concentration lower than 0.03 atoms per formula unit and assuming a full occupancy for both the sites. In addition, for monazite-(Ce), the atomic displacement parameters (*ADP*) of the oxygen atoms were refined as isotropic. All the refinements converged with no significant

Table 1. Average (and range of the measured) chemical composition (expressed in oxide wt.% and in atoms per formula unit (apfu) calculated on the basis of 4 oxygen atoms) of the chernovite-(Y), xenotime-(Y) and monazite-(Ce) samples under investigation

	Chernovite-(Y)*		Chernovite-(Y)**		Xenotime-(Y)***		Monazite-(Ce)****	
As_2O_5	36.11	(34.77–36.91)	36.36	(30.95–42.80)	5.49	(3.45–6.81)	1.95	(1.36–2.84)
P_2O_5	5.41	(3.93–6.86)	2.30	(1.38–4.52)	28.70	(25.99–31.00)	27.71	(26.60–28.55)
SiO_2	0.82	(0.45–1.59)	2.40	(1.10–3.61)	0.34	(0–0.81)	0.24	(0.02–0.69)
V_2O_5	0.01	(0–0.05)	< 0.01	(0–0.02)	b.d.l.		b.d.l.	
CaO	0.01	(0–0.03)	0.52	(0.03–1.26)	0.01	(0–0.06)	1.19	(0.54–1.59)
Y_2O_3	33.10	(29.91–35.38)	29.20	(25.94–31.94)	39.44	(37.11–41.55)	0.54	(0.39–0.62)
La_2O_3	0.01	(0–0.05)	0.05	(0–0.20)	0.03	(0–0.12)	14.18	(12.31–15.82)
Ce_2O_3	0.13	(0.01–0.25)	0.16	(0.07–0.26)	0.07	(0–0.20)	30.84	(28.41–32.95)
Pr_2O_3	0.04	(0–0.09)	0.05	(0–0.13)	0.03	(0–0.18)	3.46	(3.09–3.93)
Nd_2O_3	0.37	(0.03–0.65)	0.57	(0.07–0.94)	0.26	(0.08–0.48)	12.88	(12.21–14.46)
Sm_2O_3	0.73	(0.55–1.06)	0.84	(0.26–1.60)	0.73	(0.43–1.04)	2.20	(1.86–2.45)
Eu_2O_3	b.d.l.		b.d.l.		b.d.l.		b.d.l.	
Gd_2O_3	2.30	(1.73–3.07)	3.02	(1.70–5.44)	3.84	(2.95–5.03)	1.41	(1.04–2.06)
Tb_2O_3	0.55	(0.39–0.60)	0.63	(0.40–0.86)	0.87	(0.68–1.07)	b.d.l.	
Dy_2O_3	5.10	(4.39–5.58)	4.51	(3.81–5.05)	6.23	(5.36–6.70)	0.27	(0.13–0.43)
Ho_2O_3	2.39	(2.09–2.78)	2.40	(1.87–3.44)	3.27	(2.65–4.14)	0.25	(0.10–0.44)
Er_2O_3	3.51	(2.98–4.24)	2.58	(1.76–3.73)	3.55	(3.13–4.13)	0.03	(0–0.22)
Tm_2O_3	0.48	(0.27–0.83)	0.37	(0–0.71)	0.46	(0–0.68)	0.07	(0–0.21)
Yb_2O_3	3.38	(1.87–5.07)	2.29	(1.24–4.58)	3.08	(2.34–3.71)	0.04	(0–0.39)
Lu_2O_3	1.29	(1.01–1.73)	1.06	(0.92–1.14)	1.56	(1.07–1.95)	0.07	(0–0.24)
PbO	0.26	(0.19–0.31)	0.16	(0–0.39)	0.25	(0.04–0.47)	0.03	(0–0.20)
ThO_2	2.40	(0.78–4.94)	7.32	(1.40–12.70)	1.89	(0.31–3.87)	2.55	(0.57–5.70)
UO_2	1.90	(1.26–2.32)	3.93	(3.95–4.27)	0.40	(0.01–0.74)	0.05	(0–0.17)
Total	100.41		100.84		100.62		100.05	
Apfu								
As	0.766		0.798		0.102		0.040	
P	0.185		0.081		0.861		0.934	
Si	0.033		0.101		0.012		0.009	
V								
Ca			0.023				0.051	
Y	0.714		0.652		0.744		0.011	
La			0.001				0.208	
Ce	0.001		0.002				0.449	
Pr							0.050	
Nd	0.005		0.008		0.003		0.183	
Sm	0.010		0.012		0.008		0.030	
Eu								
Gd	0.044		0.042		0.039		0.018	
Tb	0.007		0.008		0.010			
Dy	0.066		0.061		0.071		0.003	
Ho	0.030		0.032		0.036		0.003	
Er	0.022		0.034		0.015			
Tm	0.006		0.005		0.005			
Yb	0.042		0.029		0.033			
Lu	0.015		0.013		0.016			
Pb	0.002		0.001		0.002			
Th	0.022		0.070		0.015		0.023	
U	0.017		0.036		0.003			

*(Ca,Th)-poor chernovite in the text and Ch_{10} sample in Pagliaro *et al.* (2022a); **(Ca,Th)-enriched chernovite in the text and Ch_{13} in Pagliaro *et al.* (2022a); ***Xen_{14} sample in Pagliaro *et al.* (2022a); ****Mon_{14} sample in Pagliaro *et al.* (2022a)
b.d.l. – below detection limit

correlations among the refined variables. Refined structural models are deposited as crystallographic information files (cifs) and are available as Supplementary material (see below).

For a chernovite-(Y) sample with a slightly larger amount of Ca and Th replacing Y and REE, an *in situ* high-pressure powder XRD experiment was conducted at the P02.2 beamline of PETRA III (Hamburg, Germany) with a wavelength of $\lambda = 0.2906$ Å (42.67 keV) and a Debye-Scherrer geometry. The sample was loaded into a DAC equipped with Boehler-Almax designed diamonds of 400 μm culet size along with the pressure-transmitting medium (see Table 2 for details) and ruby spheres for pressure determination (P – uncertainty ±0.05 GPa; Mao *et al.*, 1986;

Table 2. Details pertaining to the *in situ* high-pressure and high-temperature experiments of this study

Experiment	Technique*	Wavelength (Å)	*P*-transmitting medium**	Maximum *P*/*T* (GPa/°C)	Detector type/Instrument model	Exposure time per frame (s)	Synchrotron beam-line/Institution
High-pressure experiments							
(Ca,Th)-poor chernovite-(Y) at high-*P*	SC-XRD	0.41066	He	10.71(5)	Eiger2 9M CdTe	0.2	ID15B, ESRF
(Ca,Th)-enriched chernovite-(Y) at high-*P*	PXRD	0.29060	*m.e.w.*	8.20(5)	Perkin Elmer XRD1621	***	P02.2, Petra-III
Xenotime-(Y) at high-*P*	SC-XRD	0.41029	He	30.38(5)	Eiger2 9M CdTe	0.5	ID15B, ESRF
Monazite-(Ce) at high-*P*	SC-XRD	0.29060	Ne	23.50(5)	Perkin Elmer XRD1621	1	P02.2, Petra-III
High-temperature experiments							
(Ca,Th)-poor chernovite-(Y) at high-*T*	SC-XRD	0.71359	–	790(5)	Stoe IPDS II	5.5	IMP#
(Ca,Th)-enriched chernovite-(Y) at high-*T*	PXRD	0.7293	–	1000(5)	Scintillator	***	MCX, Elettra
Xenotime-(Y) at high-*T*	SC-XRD	0.71359	–	790(5)	Stoe IPDS II	2	IMP#
Monazite-(Ce) at high-*T*	SC-XRD	0.71359	–	790(5)	Stoe IPDS II	2	IMP#

*SC-XRD: single-crystal X-ray diffraction; PXRD: powder X-ray diffraction
**He: helium (Klotz *et al.*, 2009); Ne: neon (Klotz *et al.*, 2009); *m.e.w.*: methanol:ethanol:water = 16:3:1 (Angel *et al.*, 2007)
***See the text for further details
#Institute of Mineralogy and Petrography, University of Innsbruck, Austria

Chervin *et al.*, 2001). The data collection strategy at any pressure point consisted of a 30° rotation along ω, for an exposure time of 60 s. The X-ray diffraction signals captured by the Perkin Elmer XRD1621 flat panel detector have been finalised and integrated by means of the *Dioptas* software (Prescher and Prakapenka, 2015), in order to remove the background noise due to DAC components and extract the 2θ-intensity pattern for any experimental dataset. The unit-cell parameters were determined by fitting the powder XRD data by means of the Rietveld full-profile method using the *GSAS-II* software (Toby and Von Dreele, 2013): the unit-cell parameters, crystallite size, individual scale factor and profile parameters (pseudo-Voigt function) have been refined. Moreover, the background signal has been interpolated through a Chebychev polynomial function, with 4 to 15 terms.

In situ high-temperature experiments

In situ high-temperature single-crystal X-ray diffraction data were collected at the Institute of Mineralogy and Petrography of the University of Innsbruck, using a Stoe IPDS II diffractometer equipped with a Heatstream H*T* device, providing a continuous flow of hot N_2. The primary X-ray beam was generated by an X-ray tube (Mo-anode), operating at 50 kV and 40 mA. A plane graphite monochromator and a multiple pinhole collimator (0.5 mm) were used to guide the beam onto the sample. The image-plate detector was placed at a distance of 100 mm. The temperature calibration had been conducted previously using phase transitions of KNO_3, Ag_2SO_4, K_2SO_4 and K_2CrO_4 powders into glass capillaries. The samples, single crystals of monazite-(Ce), xenotime-(Y) and chernovite-Y (ca. 50–120 μm^3) have been inserted into SiO_2 glass capillaries (0.1 mm in diameter). For all the samples, the data collection consisted in a 180° ω-rotation with a step size of 1° and variable exposure times. The temperature accuracy is ≤ 5°C. Further details about the experimental setting are reported in Krüger and Breil (2009). Data collection and reduction has been performed using X-Area (Stoe and Cie, 2008). The indexed cell parameters were always compatible with either the unit cells of chernovite-(Y), xenotime-(Y) or monazite-(Ce).

Structure refinements were performed based on the single-crystal XRD data adopting the same procedure reported previously for the high-pressure data, and refined structural models are available as cifs (supplementary materials, see below). The thermal evolution of significant structural parameters (*i.e.* *A*–O bonds, *A*-coordination polyhedral and *T*-coordination polyhedral volumes) has been determined from the refined structure models, by means of the tools implemented in the *VESTA3* software (Momma and Izumi, 2011).

In situ high-temperature X-ray powder diffraction experiments were performed on the chernovite sample relatively enriched in Ca and Th at the MCX beamline of the Elettra synchrotron (Basovizza, Trieste Italy), with a wavelength of $\lambda = 0.7293$ Å (17 keV) and a Debye-Scherrer setting. The sample, ground to powder in an agate mortar, was loaded in a SiO_2 glass capillary (0.3 mm as outer diameter). For any experimental point, the data collection strategy consisted of a 2θ-scan between 8° and 60°. A step size of 0.008° was applied and an equivalent counting time for 1 s/step used. The X-ray diffraction effects were collected by the high-resolution scintillator detector available at the beamline. During the data collection, the sample was spun at a rate of 1000 rotations per minute along the φ-axis. The sample was heated by an air blower, operating between 30 and 1000°C. Further details concerning the experimental setting are reported in Rebuffi *et al.* (2014) and Lausi *et al.* (2015).

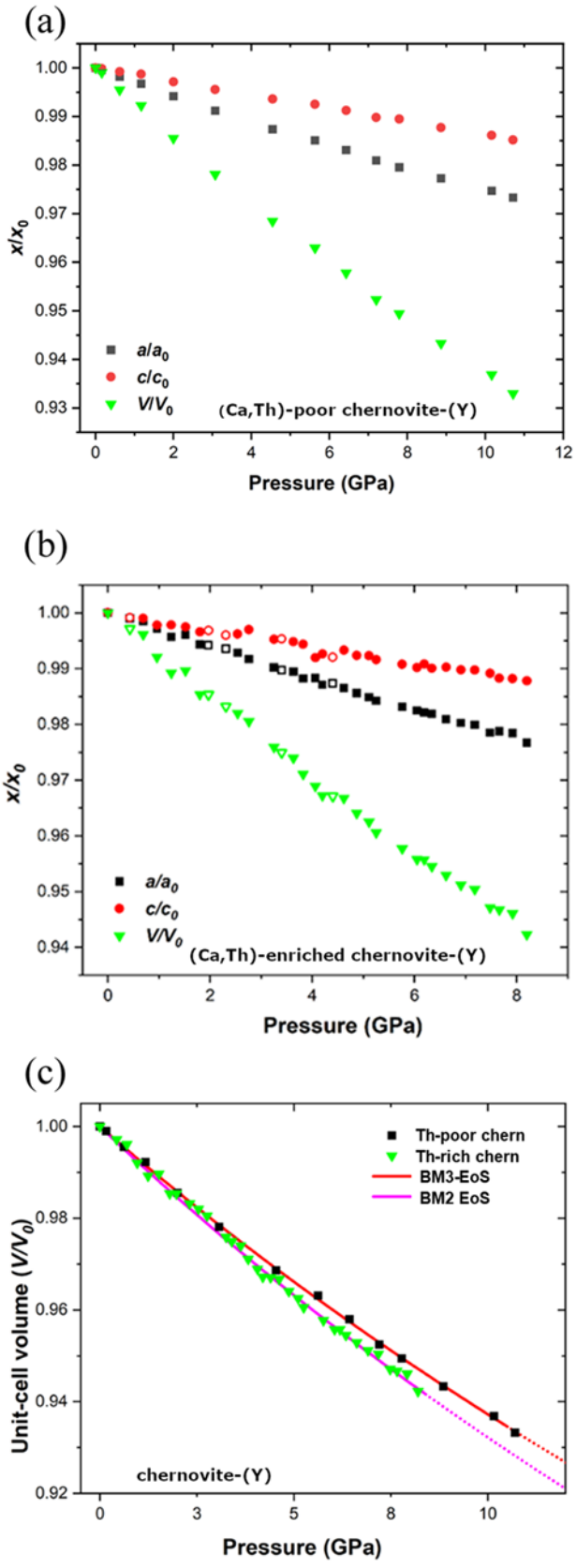

Figure 4. High-pressure evolution of the unit-cell parameters (normalised to ambient conditions values) of (a) the investigated (Ca,Th)-poor and (b) (Ca,Th)-enriched chernovite-(Y) samples and (c) of their respective normalised unit-cell volumes with the refined Birch-Murnaghan equations of state. Empty symbols refer to data collected in decompression.

Results and discussion

Compressional behaviour of the REETO$_4$ minerals

The evolution of the unit-cell parameters of the investigated samples with pressure is reported in Table S3 and shown in Figs 4 and 5. For monazite-(Ce), the evolution of unit-cell parameters *vs. P* shows no evidence of phase transformation in the entire *P*-range investigated. Both the zircon-type minerals, on the other hand, show the occurrence of a phase transition. Chernovite-(Y), at pressures higher than ~10 GPa is no longer stable, undergoing a phase transition to several single-crystal fragments, for which, the position of the peaks in the XRD pattern is compatible with a tetragonal scheelite-type structure. Otherwise, at pressures exceeding ~17 GPa, xenotime-(Y) undergoes a single-crystal to single-crystal phase transition towards a monazite-type structure. For any pressure ramp, the elastic behaviour of the mineral studied has been described by fitting an isothermal Birch-Murnaghan EoS (BM-EoS), truncated at the second or third order, to the *P*–*V* data (a comprehensive description of the BM-EoS formalism can be found in Angel, 2000) using the *EoS-Fit7_GUI* software (Gonzalez-Platas *et al.*, 2016). For monazite, similarly to what was observed for the isostructural gasparite-(Ce) by Pagliaro *et al.* (2022b), a change in the compressional behaviour was detected at ~18 GPa. The parameters refined by fitting the experimental data by BM-EoS are reported in Table 3, among them: the bulk modulus $K_V = \beta_V^{-1} = -V^*(\partial P/\partial V)$ and its pressure derivative $K_V' = (\partial K_V/\partial P)_T$.

The evolution of significant structural parameters (*i.e.,* *A*–O bonds, *A*-coordination polyhedral and *T*-coordination polyhedral volumes) with pressure has been determined, based on the refined structure models, by using the *VESTA3* software (Momma and Izumi, 2011). The corresponding values are reported in Table S4.

The results of this study confirm that arsenates are always more compressible than the isostructural phosphates (Table 3), in agreement with the observed relationship that the larger the ionic radii of the *A* and *T* sites, the higher the bulk compressibility (*e.g.* Zhang *et al.*, 2008; Li *et al.*, 2009; Lacomba-Perales *et al.*, 2010; Errandonea *et al.*, 2011). The refined bulk moduli apparently suggest that monazite-structure type minerals are more compressible than those with a zircon-structure type (Table 3). However, internally consistent theoretical data (Zhang *et al.*, 2008; Li *et al.*, 2009) show that there is a clear increase in compressibility along the lanthanoid series from Lu to La, with a discontinuity in the form of a stiffening when transforming from the zircon to the monazite structure type. Therefore, it can be concluded that, for the investigated minerals, the softening induced by the larger *A* site has a stronger impact than the stiffening induced by the monazite structure type.

The two minerals investigated, with the same zircon structure type, *i.e.* chernovite-(Y) and xenotime-(Y), undergo different phase transitions paths. Chernovite-(Y) experiences an irreversible transition, from a single-crystal to several crystal fragments, towards a scheelite-type polymorph between ca. 10.5 and 11 GPa. The same phase transition occurs, for synthetic $YAsO_4$ in a powder XRD experiment, in a broader pressure range between 8 and 12 GPa (Errandonea *et al.*, 2011). The apparent discrepancy between these two studies may be ascribed to: (1) a different kinetics of the phase transition between a single crystal and a polycrystalline material; and (2) slightly different chemical compositions, as a higher phosphorous content in the presently investigated mineral decreases the average radius of the *T* site; or a combination of both. In general, the same phase transition has already been

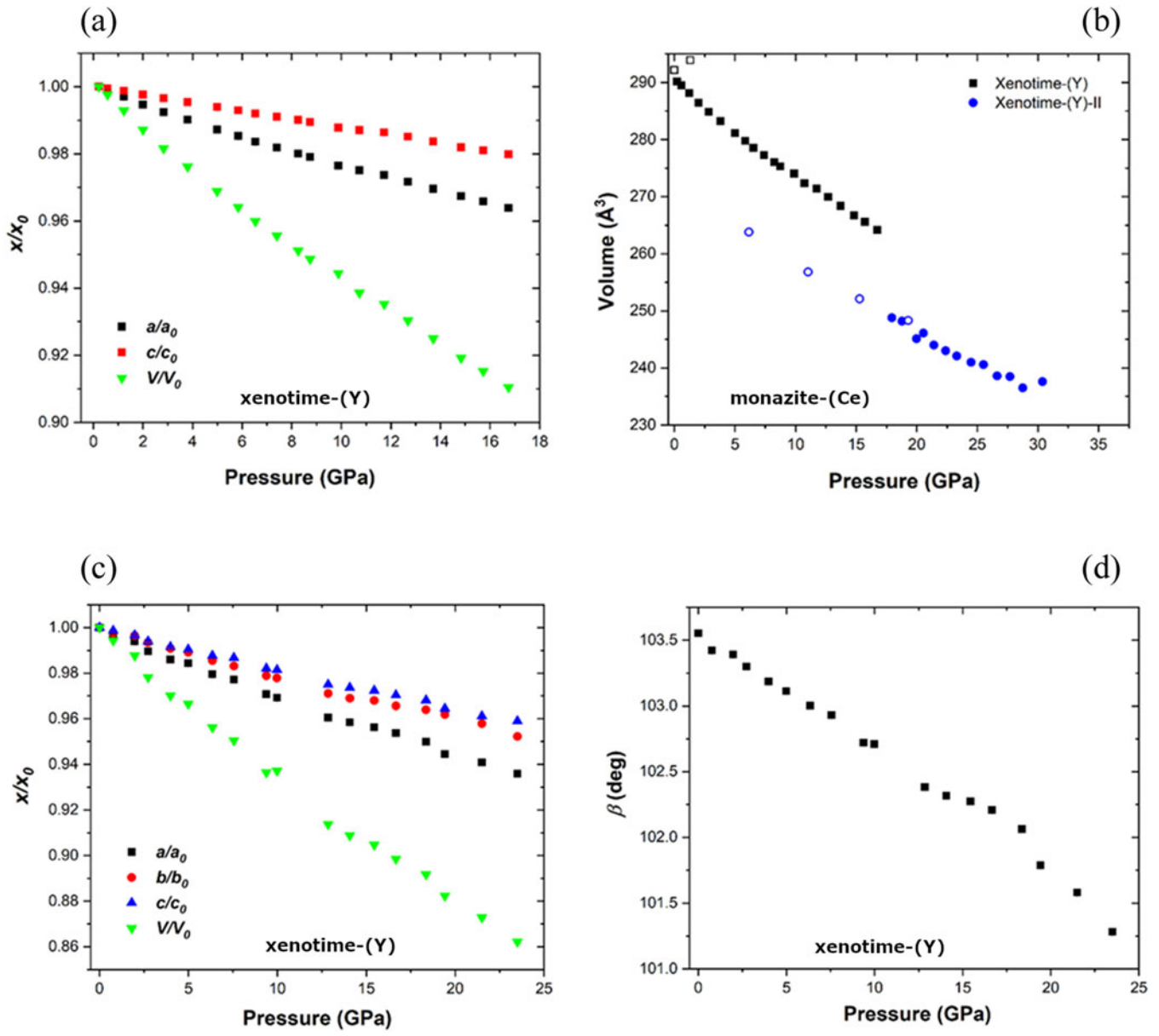

Figure 5. High-pressure evolution of the unit-cell parameters (normalised to ambient-conditions values) of (a) xenotime-(Y) and (c) monazite-(Ce), (b) the normalised unit-cell volumes of the ambient-pressure and high-pressure polymorphs of xenotime-(Y) and (d) of the monoclinic β angle of monazite-(Ce).

observed to occur in other ATO_4 compounds, where the pressure of transition increases with the decrease of the *A* and *T* atoms ionic radii (Wang *et al.*, 2004; Zhang *et al.*, 2009; Lacomba-Perales *et al.*, 2010; Errandonea *et al.*, 2011). The relationship between the ionic radii of the *A* and *T* atoms and the type of structure stable at ambient and high-pressure conditions is well known and was first described by Fukunaga and Yamaoka (1979) and Bastide (1987), and later discussed in other publications, *e.g.* in Lopez-Solano *et al.* (2010). As suggested by the Bastide diagram (Fig. 1) and already reported in the literature (Tatsi *et al.*, 2008; Zhang *et al.*, 2009; Lacomba-Perales *et al.*, 2010; Musselman, 2017; Heuser *et al.*, 2018), xenotime-(Y) and isomorphous phosphates undergo a single-crystal to single-crystal phase transition towards a high-pressure polymorph, xenotime-(Y)-II, showing a monazite-type structure. The transition observed in our experiments occurs at a pressure (> 17 GPa) consistent with those reported for synthetic YPO_4 compounds (Zhang *et al.*, 2008; Lacomba-Perales *et al.*, 2010). The reversibility of this phase transition is confirmed by this single-crystal study, even though with a significant hysteresis, as the tetragonal polymorph is recovered in decompression only between 6.3 and 1.3 GPa.

Despite a relative scattering between the published values of bulk compressibilities of zircon- and monazite-type phosphates and arsenates, determined on the basis of experimental and theoretical studies, the elastic parameters refined for the mineral species of this study (Table 3) are in agreement with those reported in the literature (Table S1). In the zircon-type minerals chernovite-(Y) and xenotime-(Y), the bulk compression is significantly anisotropic. Indeed, the structure is approximately two times more compressible within the (001) plane than along [001] (Figs 4 and 5, Table S5), which corresponds to the direction of the polyhedral chains evolution. Such a behaviour is strongly

Table 3. Refined equations of state parameters from the fit to the experimental high-pressure and high-temperature unit-cell volume data (see text for further details)

High-pressure experiments							
	BM3 EoS				BM2 EoS		
	K_{V0} (GPa)	β_V (GPa^{-1})	K_V'	V_0 ($Å^3$)	K_{V0} (GPa)	β_V (GPa^{-1})	V_0 ($Å^3$)
(Ca,Th)-poor chernovite-(Y)	136(2)	0.0074(1)	4.0(5)	310.43(3)	135.5(5)	0.00738(1)	310.43(3)
(Ca,Th)-enriched chernovite-(Y)	125(3)	0.0080(1)	3.8(9)	316.16(9)	123.8(9)	0.00808(7)	316.17(7)
Xenotime-(Y)	145(4)	0.0068(2)	4.4(5)	290.4(2)	148(1)	0.00676(5)	290.4(1)
Monazite-(Ce)	–	–	–	–	121(3)	0.0083(2)	299.3(4)
Gasparite-(Ce)*	109(4)	0.0092(3)	4.3(6)	320.6(3)	105(1)	0.00951(9)	320.7(2)
High-temperature experiments							
	Holland-Powell EoS				1st order polynomial fit		
	α_V ($\times10^{-6}$ K^{-1})	a_0 ($\times10^{-5}$ K^{-1})	a_1 ($\times10^{-4}$ $K^{-1/2}$)	V_0 ($Å^3$)		LTEC ($\times10^{-6}$ K^{-1})	V_0 ($Å^3$)
(Ca,Th)-poor chernovite-(Y)	9.7(1)	2.33(3)	0	307.02(3)		4.81	306.74
(Ca,Th)-enriched chernovite-(Y)	8.0(1)	1.90(2)	0	313.06(2)		3.98	312.84
Xenotime-(Y)	9.6(12)	3.5(3)	0.8(4)	288.07(4)		6.00	287.73
Monazite-(Ce)	19.9(13)	4.9(3)	0.2(4)	297.97(5)		9.73	297.50

*From Pagliaro *et al.* (2022b).
α_V: volume thermal expansion coefficient at ambient conditions calculated on the basis of the Holland-Powell EoS.
a_0 and a_1 are two refinable variables in the Holland-Powell EoS (Holland and Powell, 1998).

controlled by the high tetragonal symmetry, which limits the intra-chain deformation, as confirmed by the behaviour of the two independent *A*–O bond distances, where the *A*–O_a bonds, oriented parallel to [001] (Fig. 2), are the less compressible in both the minerals (Table S4). The bulk compression is therefore mainly accommodated by the AO_8 coordination polyhedron, as suggested by its bulk modulus, refined by modelling the polyhedral volume data obtained using *Vesta3* with a II-BM equation of state by means of the *EoS-Fit7-GUI* software (Table 4). For both chernovite-(Y) and xenotime-(Y), bulk moduli values of the *A*-polyhedra are much lower than those obtained for the AsO_4 and PO_4 tetrahedra, which behave as quasi-rigid units (Table 4). The same conclusion can be drawn for monazite-(Ce) (Table 4) and gasparite-(Ce) (Pagliaro *et al.*, 2022b), which, in addition, show that the AsO_4 tetrahedra are slightly more compressible than the PO_4 ones. As observed previously by Pagliaro *et al.* (2022a), the structural features (and responses to external *T* and *P* stimuli) of these compounds are strongly controlled by the crystal chemistry, in particular of the *T* sites. Moreover, not only do PO_4 and AsO_4 tetrahedra have a different compressional behaviour, but the nature of the prevailing *T* site controls the size (*i.e.* the average ionic radius) at ambient conditions of the *A* polyhedron (Pagliaro *et al.*, 2022a). This leads, given a similar chemical composition of the *A* site, to slightly larger compressibility for the more 'expanded' *A*-polyhedra of the arsenates among isostructural minerals. The control exerted by the crystal chemistry on the elastic response is also pointed out by the chernovite sample relatively enriched in Ca and Th studied here, which shows a slightly lower bulk modulus value (Table 3). The lack of structure refinements prevents an unambiguous derivation of the structural mechanisms responsible for this behaviour, but it can be suggested that the more 'expanded' *A*-polyhedron (due to the higher content of the larger Th and Ca ions, as reported in Table 1) is coherent with the previous observations that a larger average ionic radius of the *A* site generates a softer polyhedron.

The description of the elastic anisotropy in monazite-(Ce) is less straightforward, as the monoclinic symmetry does not allow us to rely on the axial compressibilities alone, given the variation of the β angle with pressure. Therefore, the finite Eulerian unit-strain tensor of monazite-(Ce) between ambient-*P* and 18.39 GPa has been calculated using the *Win_Strain* software (Angel, 2011) and with a geometric setting with $X//a^*$ and $Y//b$. The results show that the principal axes of maximum and minimum unit-strain do not correspond with any of the crystallographic axes, as described by the tensor values in the following matrix:

$$\begin{pmatrix} \varepsilon_1 \\ \varepsilon_2 \\ \varepsilon_3 \end{pmatrix} \begin{pmatrix} 158.2\,(2)^\circ & 90^\circ & 56.2\,(2)^\circ \\ 90^\circ & 180^\circ & 90^\circ \\ 68.2\,(2)^\circ & 90^\circ & 33.8\,(2)^\circ \end{pmatrix} \cdot \begin{pmatrix} a \\ b \\ c \end{pmatrix}$$

The analysis of the finite Eulerian unit-strain tensor allowed the determination of the mean compressibility values along the axes of the strain ellipsoid (with $\varepsilon_1 > \varepsilon_2 > \varepsilon_3$): $\varepsilon_1 = 0.003030(11)$ GPa^{-1}, $\varepsilon_2 = 0.00200(2)$ GPa^{-1}, $\varepsilon_3 = 0.0014(12)$ GPa^{-1}. The directions of minimum and maximum compressibility are within the (010) plane and the anisotropic scheme is $\varepsilon_1:\varepsilon_2:\varepsilon_3$=2.16:1.43:1. A comparison with the finite Eulerian unit-strain tensor reported for gasparite-(Ce) by Pagliaro *et al.* (2022b) points out that these isostructural minerals share a similar elastic anisotropy. The shared compressional behaviour extends to the structural deformation mechanisms acting on the atomic scale: the nine independent *A*–O bond distances in monazite-(Ce) have different compressional evolutions, as shown in Fig. 6 (see also Table S4). A moderate scattering of the monazite-(Ce) unit-cell parameters can be observed between 10 and 18 GPa, which implied that we should fit the *V*–*P* data using a Birch-Murnaghan equation of state truncated to the II-order (Table 3). On the basis of the available experimental data and structure refinements, it is not possible to unambiguously detect a change in the compressional behaviour at $P < 18$ GPa. On the contrary, a change in the response to compression clearly occurs at pressures exceeding ~18.4 GPa, as evidenced by the significant deviation in the high-pressure evolution of the monoclinic β angle (Fig. 5; Table S3), similar to gasparite-(Ce) (Pagliaro *et al.*, 2022b). This behaviour has already been reported

Table 4. Refined equation-of-state parameters pertaining to the *A*- and *T*-sites coordination polyhedra from the high-pressure (BM2 EoS) and high-temperature (Holland-Powell EoS, only *A*-site coordination polyhedron) experiments

High-pressure experiments				
	$K_{V(AO8/AO9)}$ (GPa)	$V_{0(AO8/AO9)}$ (Å^3)	$K_{V(TO4)}$* (GPa)	$V_{0(TO4)}$ (Å^3)
(Ca,Th)-poor chernovite-(Y)	120(12)	23.53(9)	262(56)	2.319(10)
Xenotime-(Y)	126(4)	23.18(4)	299(62)	1.900(9)
Xenotime-(Y)-II	87(26)	30.4(12)	–	–
Monazite-(Ce)	110(4)	32.45(8)	395(130)	1.863(12)
Gasparite-(Ce)**	99(3)	33.02(4)	–	–
High-temperature experiments				
	$\alpha_{V(AO8/AO9)}$ (x10^{-6} K^{-1})	a_0 (x10^{-5} K^{-1})	a_1 (x10^{-4} K$^{-1/2}$)	$V_{0(AO8/AO9)}$ (Å^3)
(Ca,Th)-poor chernovite-(Y)	16(3)	3.8(7)	0	23.49(4)
Xenotime-(Y)	18(2)	4.2(5)	0	23.03(4)
Monazite-(Ce)	25(2)	6.0(5)	0	32.36(4)

*Due to the high uncertainties, these data should be considered as a qualitative estimation of the TO_4 units rigid behaviour
**From Pagliaro *et al.* (2022b)

for synthetic monazite-type $LaPO_4$ and $CePO_4$ (Huang *et al.*, 2010), but not in another high-pressure investigation of $CePO_4$ (Errandonea *et al.*, 2018). The structure refinements performed in this study allows us to draw a relationship between the change in the elastic behaviour and the structural re-configuration. Figure 6 and Table S4 show that, at lower pressures, the O_{3c} atom is too far from the *A* site to be considered to effectively belong to its coordination sphere (Fig. 3). However, the A–O_{3c} interatomic distance shows a significant shortening under compression (Fig. 6; Table S4), so that, at a pressure consistent with the change in the compressional behaviour, the O_{3c} atom is close enough to the *A* site to enter its coordination sphere, as suggested by the individual bond valences calculated for selected structure refinements and reported in Table S6. As a consequence, the coordination number of the *A* site would increase from 9 (8+1) to 10 (8+2), even though with different contributions from the individual bonds, given the longer bond distances of the of A–$O2_a$ and A–$O3_c$ (Tables S4 and S6). As the same behaviour has already been independently described for gasparite-(Ce) (Pagliaro *et al.*, 2022b) and is analogous to what is described to occur at 3.25 GPa in the monazite-type crocoite ($PbCrO_4$, Bandiello *et al.*, 2012; Errandonea and Kumar, 2014), we are inclined to believe that this is an intrinsic feature of the monazite structure type. Therefore, the known transition to a post-baryte-type polymorph at *P* higher than 26 GPa (Ruiz-Fuertes *et al.*, 2016) is accomplished through an intermediate structural configuration, still preserving the monazite symmetry and atomic arrangement, but characterised by an increase from 9 to 10 in the number of the oxygen atoms bonded to the lanthanide-bearing site. This intermediate structural configuration is accomplished, with no clear discontinuity, by a smooth approach of the $O3_c$ atom to the *A* site (where $O3_c$ corresponds to $O3_a$ and $O3_b$ in the coordination sphere of two further *A* atoms). It is worth noting, that the same configuration, with a 10-fold coordinated *A*-site, is also shared by the monazite-type high-pressure polymorph of $CaSO_4$ (Crichton *et al.*, 2005). The higher pressure at which the change of the elastic behaviour occurs in monazite-(Ce) (ca. 18.4 GPa, *vs.* ca. 15 GPa in gasparite-(Ce), Pagliaro *et al.*, 2022b) is consistent with the higher *P*-stability expected for the isostructural phosphate with smaller average atomic radii.

Despite being affected by larger experimental uncertainties, the same deformation mechanisms described for monazite-(Ce) and gasparite-(Ce) can be derived by the analysis of the refined structural models of the monazite-type high-pressure xenotime-(Y)-II polymorph (Table S4). In this case, the possible occurrence of a change in the compressional behaviour, according to the previous description, should be verified by investigations performed up to higher pressure values, though interatomic A–$O3_c$ bond distances of ~2.8–2.9 Å (Table S4) can suggest a 10-fold coordinated *A* site. A striking and anomalous feature shown by the experimental results of this study concerns the much larger refined compressibility if compared to what is reported in other studies for the same polymorph (K_V = 146(5) GPa in this study; K_V = 206 and 266 GPa in Zhang *et al.* (2009) and Lacomba-Perales *et al.* (2010), respectively). The relatively high number of experimental data of this study leads us to the conclusion that the refined bulk modulus value we obtained is very reliable, implying a similar compressibility between the ambient and high-pressure polymorphs of the investigated xenotime-(Y). It is worth mentioning that a similar compressibility can also be found between the zircon- and monazite-type polymorphs of $LaVO_4$, with K_{V0} = 93(2) GPa (Yuan *et al.*, 2015) and 95(5) GPa (Errandonea *et al.*, 2016), respectively. The thorough re-investigation of the zircon-to-monazite phase transition in xenotime and of the elastic behaviour of the xenotime-II polymorphs appear, therefore, mandatory for a comprehensive understanding.

Thermal behaviour of the REETO$_4$ minerals

The thermal unit-cell parameters evolution from the three *in situ* single-crystal high-*T* ramps on monazite-(Ce), chernovite-(Y) and xenotime-(Y) and from the powder ramp on chernovite-(Y), relatively enriched in Ca and Th, are reported in Table S7 and shown in Fig. 7. The thermo-elastic behaviour has been modelled according to the isobaric equation of state modified from Pawley *et al.* (1996) and Holland and Powell (1998) and implemented in the *EoS-Fit7_GUI* (Gonzalez-Platas *et al.*, 2016). The linear thermal expansion coefficients have also been refined using the *TEV* software (Langreiter and Kahlenberg, 2015). The refined parameters and the calculated thermal expansion coefficients at ambient conditions $\alpha_V = 1/V^*(\partial V/\partial T)_P$ are reported in Table 3.

A comparison of the linear thermal expansion coefficients refined in this study for xenotime-(Y) and monazite-(Ce) and those already published for the same compounds reveal a good agreement with the literature data (see Table S2 and references therein). However, a significant discrepancy is observed between

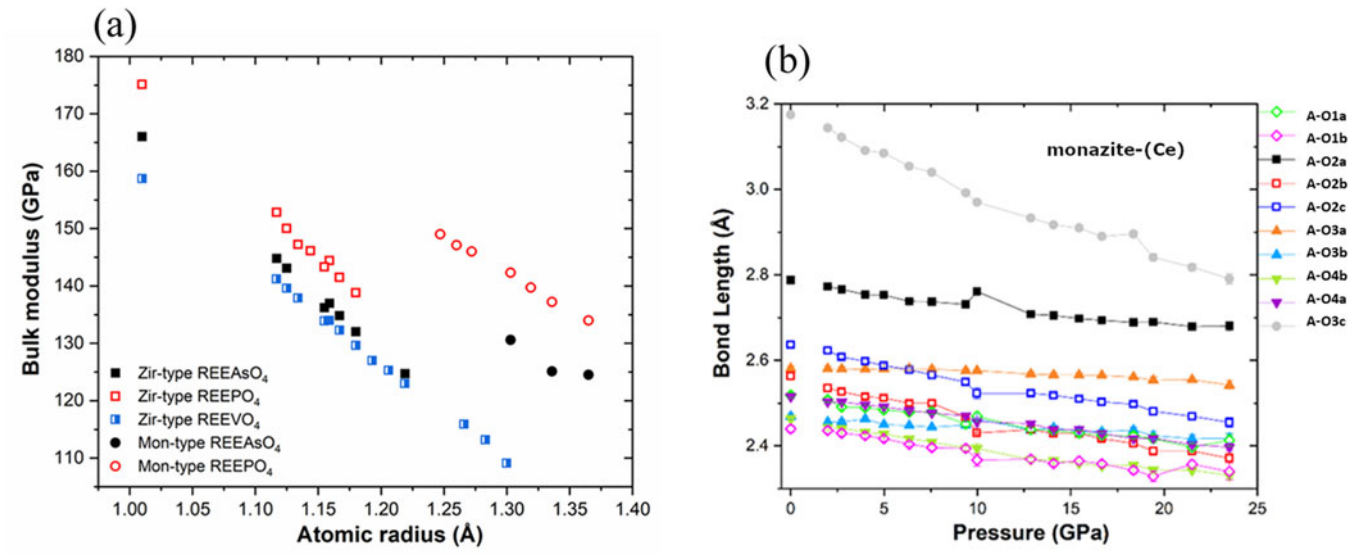

Figure 6. (a) Bulk moduli as a function of the *A*-site atomic radii for several REETO_4 (T = As,P,V) minerals, after Li *et al.* (2009) and Zhang *et al.* (2008). (b) High-pressure evolution of the *A*–O interatomic bond distances in monazite-(Ce).

the values refined for chernovite-(Y) in this study and those reported previously by experimental investigations of $YAsO_4$ (Kahle, 1970; Schopper, 1972; Reddy *et al.*, 1988). As none of the cited references provide experimental unit-cell parameters, nor structure refinements, it is not possible to discuss such a discrepancy, but it is worth noting that the refined values for both the (Ca,Th)-poor and (Ca,Th)-enriched chernovites of this study are self-consistent and diverge from the literature data. With this in mind, future investigation of other natural or synthetic $YAsO_4$-type zircon compounds seems imperative.

A comparative analysis of the thermo-elastic behaviour of the investigated minerals shows that monazite-(Ce) is much more expansible than the two zircon-type compounds (Table 3). In the latter, the [001] direction, *i.e.* the least compressible at high-P, is found to be the most expansible at high-T. The thermo-elastic anisotropy of monazite-(Ce) cannot be directly described based on the unit-cell parameters behaviour, given its monoclinic symmetry. The thermal expansion of monazite-(Ce) has been modelled with the *TEV* software (Langreiter and Kahlenberg, 2015) and at the temperature of 400°C (*i.e.* $\Delta T \sim$ 380°C) its relationship with the unit-cell axes, with a geometric setting with $X//a^*$ and $Y//b$, is described by the following matrix:

$$\begin{pmatrix} \alpha_1 \\ \alpha_2 \\ \alpha_3 \end{pmatrix} \angle \begin{pmatrix} 109.02^\circ & 90^\circ & 5.47^\circ \\ 19.02^\circ & 90^\circ & 84.53^\circ \\ 90^\circ & 0^\circ & 90^\circ \end{pmatrix} \cdot \begin{pmatrix} a \\ b \\ c \end{pmatrix}$$

The mean thermal expansivity along the axes of the unit-strain ellipsoid, determined at 400°C, is: $\alpha_1 = 11.56 \cdot 10^{-6}$ K^{-1}, $\alpha_2 = 9.93 \cdot 10^{-6}$ K^{-1} and $\alpha_3 = 7.39 \cdot 10^{-6}$ K^{-1}, leading to the anisotropic scheme α_1: α_2: α_3 = 1.56:1.34:1.

The structure refinements (thermal evolution of selected structural parameters is reported in Table S8) showed that for the zircon-type minerals xenotime-(Y) and chernovite-(Y), the coordination polyhedron hosting the lanthanides ions (*A*-polyhedron) has a paramount role in accommodating the bulk thermal expansion, its refined thermal expansivity being almost the double of the value referred for the unit-cell volume (Tables 3, 4), whereas the two independent *A*–O bond distances show a comparable behaviour, different to what is shown at high-P (Table S8). In monazite-(Ce) as well, the *A*-polyhedron plays a significant role in accommodating the thermal expansion, but of a lesser magnitude with respect to the tetragonal minerals (Tables 3, 4), given the larger degrees of freedom for structure deformation induced by the monoclinic symmetry. In all the cases, it is worth noting that the tetrahedra, being either PO_4 or AsO_4, appear to behave as rigid units in the temperature range investigated (Table 4).

As a general observation based on the experimental data of this study, xenotime-(Y) appears more expansible with temperature than chernovite-(Y). Even though the discrepancy between our data and the previously published thermal expansion behaviour of other $YAsO_4$ compounds (Kahle, 1970; Schopper, 1972; Reddy *et al.*, 1988) suggests caution in this regards. However, our observation is consistent with the results reported by Li *et al.* (2009) for APO_4 and $AAsO_4$ (A = lanthanides) and based on theoretical calculations of lattice energies, where phosphates always show a larger expansibility than isostructural arsenates sharing the same A cation for both the zircon and monazite structural types.

Concluding remarks

The experimental data reported in this study, along with those published by Pagliaro *et al.* (2022b) on the high-pressure behaviour of gasparite-(Ce), provide a suite of thermo-elastic parameters for natural lanthanide-bearing phosphates and arsenates cropping out in the hydrothermal veins of the Mt. Cervandone.

Consistently with the previous scientific literature, the two zircon-type minerals undergo different P-induced phase transitions. Chernovite-(Y), above ~10 GPa converts to a scheelite-type polymorph, whereas xenotime-(Y), above ~17 GPa, transforms into a monazite-type polymorph by a reconstructive phase transition, single-crystal to single-crystal in character.

The monazite-type phosphates and arsenates do not undergo any phase transitions in the explored pressure range of this study.

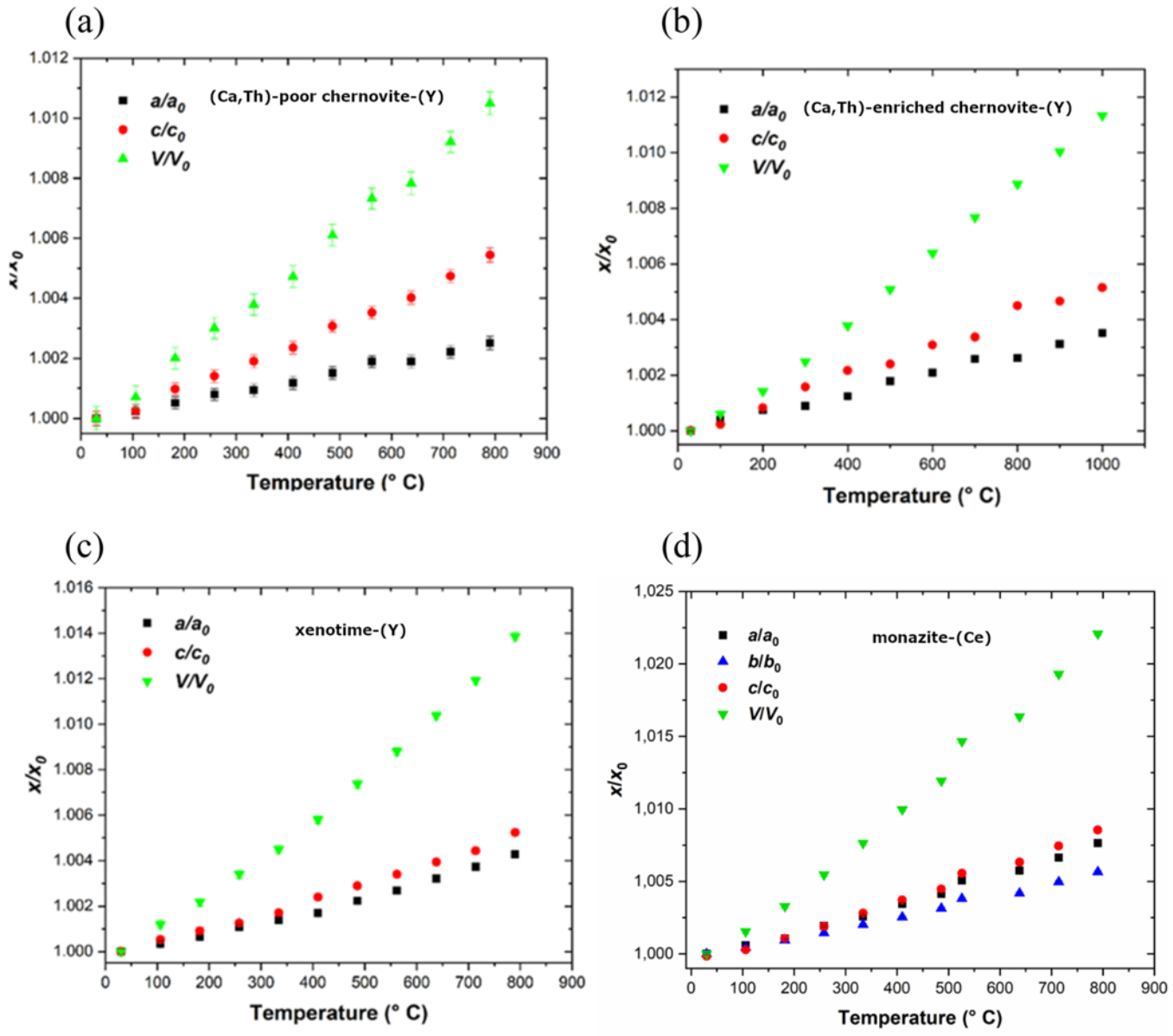

Figure 7. High-temperature evolution of the unit-cell parameters (normalised to ambient-conditions values) of (a) (Ca,Th)-poor and (b) (Ca,Th)-enriched chernovite-(Y), (c) xenotime-(Y) and (d) monazite-(Ce).

However, the analysis of the compressional evolution of the unit-cell parameters and of the crystal structures of monazite-(Ce) (this study) and gasparite-(Ce) from the same locality (Pagliaro *et al.*, 2022b), highlighted a change in the compressional behaviour occurring at ~18 and 15 GPa, respectively. This is related, for both the minerals, to a structural re-arrangement involving the smooth approach of a tenth oxygen atom into the coordination sphere of the lanthanide-bearing *A* site, which increases its coordination from 9 (8+1) to 10 (8+2) before the expected phase transition to a high-pressure polymorph. A general conclusion from both the present experiments and previous studies is that, despite the numerous papers publishing high-quality data on these crystalline compounds relevant to Earth and Materials sciences, there are still unexplored regions, whose physical-chemical features should be described by the adoption of up-to-date experimental techniques, facilities and crystallographic methods.

The analysis of the elastic and structural response with pressure and temperature of the investigated minerals of this study, combined with those on gasparite-(Ce) (Pagliaro *et al.*, 2022b), lead us to conclude that their compressional and thermal behaviours are not, as commonly observed, induced by the same mechanisms opposite in sign. For example, phosphates are less compressible than the isostructural arsenates, but at high temperature they are *more* expansible. In the same way, the zircon-type structure is less compressible along the **c** crystallographic direction, but at high-*T* along the same direction the higher expansivity is shown. This behaviour can be explained by the significant control exerted on these compounds by the chemical strain. As described by Pagliaro *et al.* (2022a), the chemical nature of the *T* cations (P or As) has a paramount role in controlling not only the TO_4 tetrahedra, but also the other structural parameters: the substitution of P by As not only expands the tetrahedron, but the *A* coordination polyhedron

too (at the same chemical composition of the *A* site). This study shows that the chemically more 'expanded' structures of the arsenates are more compressible than the chemically more 'compressed' structures of phosphates, but in response to a thermal perturbation they show the opposite behaviour being less expansible. Such an observation is confirmed by the slightly different behaviours of the two investigated chernovite samples. The sample relatively enriched in Th and Ca, due to the larger ionic radii of these cations with respect to the dominant Y in the *A* site, show a chemical expansion at ambient conditions (as described in Pagliaro *et al.*, 2022a) that is reflected by a slightly larger compressibility at high pressure and a slightly lower expansivity at high temperature.

Supplementary material. The supplementary material for this article can be found at https://doi.org/10.1180/mgm.2024.70.

Acknowledgements. This manuscript is dedicated to the memory of our friend and colleague Dr. Alessandro Guastoni (1966–2022), who has given a significant contribution in the conceptualization of this study. FP, GDG and PL are grateful to Alessandro for the numerous and fruitful discussions on this and many other topics. The editors and two anonymous reviewers are acknowledged for the handling of the manuscript and for the fruitful and insightful comments. We acknowledge DESY (Hamburg, Germany), a member of the Helmholtz Association HGF, for the provision of experimental facilities. Parts of this research were carried out at PETRA III. Beamtime was allocated for proposals I-20210452 EC and I-20211179 EC. We acknowledge Elettra Sincrotrone Trieste for providing access to its synchrotron radiation facilities. We acknowledge the European Synchrotron Radiation Facility (ESRF) for provision of synchrotron radiation facilities. The research leading to this result has been supported by the project CALIPSOplus under Grant Agreement 730872 from the EU Framework Programme for Research and Innovation HORIZON 2020. FP, DC, TB, GDG and PL acknowledge the Italian Ministry of University for the support through the project "Dipartimenti di Eccellenza 2023–2027". DC, GDG and PL acknowledge the University of Milan for the support through the project "Piano di sostegno alla Ricerca 2022".

Competing interests. The authors declare none.

References

Angel R.J. (2000) Equations of State. Pp. 35–59 in: *High-Temperature and High Pressure Crystal Chemistry* (Robert M. Hazen and Robert T. Downs, editors). Reviews in Mineralogy and Geochemistry, **41**. The Mineralogical Society of America and the Geochemical Society, Chantilly, Virginia, USA, doi: 10.2138/rmg.2000.41.2

Angel R.J. (2011) *Win_Strain: A program to calculate strain tensors from unit-cell parameters*. http://www.rossangel.com/home.htm

Angel R.J., Bujak M., Zhao J., Gatta G.D. and Jacobsen S.D. (2007) Effective hydrostatic limits of pressure media for high-pressure crystallographic studies. *Journal of Applied Crystallography*, **40**, 26–32, doi: 10.1107/S0021889806045523.

Bandiello E., Errandonea D., Martinez-Garcia D., Santamaria-Perez D. and Manjón F.J. (2012) Effects of high-pressure on the structural, vibrational, and electronic properties of monazite-type $PbCrO_4$. *Physical Review B*, **85**, 024108, doi: 10.1103/PhysRevB.85.024108.

Bastide J.P. (1987) Systématique simplifiée des composés ABX_4 ($X = O^{2-}, F^-$) et evolution possible de leurs structures cristallines sous pression. *Journal of Solid State Chemistry*, **71**, 115–120. doi: 10.1016/0022-4596(87)90149-6

Beall G.W., Boatner L.A., Mullica D.F. and Milligan W.O. (1981) The structure of cerium orthophosphate, a synthetic analogue of monazite. *Journal of Inorganic and Nuclear Chemistry*, **43**, 101–105. doi: 10.1016/0022-1902(81)80443-5

Binks W. (1926) The crystalline structure of zircon. *Mineralogical Magazine and Journal of the Mineralogical Society*, **21**, 176–187, doi: 10.1180/minmag.1926.021.115.06

Boatner L.A. (2002) Synthesis, structure, and properties of monazite, pretulite, and xenotime. Pp. 87–121 in: *Micas: Crystal Chemistry & Metamorphic Petrology* (Annibale Mottana, Francesco Paolo Sassi, James B. Thompson, Jr. and Stephen Guggenheim, editors). Reviews in Mineralogy and Geochemistry, 48. The Mineralogical Society of America and the Geochemical Society, Chantilly, Virginia, USA, doi: 10.2138/rmg.2002.48.4

Bragg W.L. (1929) Atomic arrangement in the silicates. *Transactions of the Faraday Society*, **25**, 291, doi: 10.1039/TF9292500291

Brown I.D. (2002) *The Chemical Bond in Inorganic Chemistry: The Bond Valence Model*. Oxford University Press, Oxford, 288 pp.

Bykova E., Aprilis G., Bykov M., Glazyrin K., Wendt M., Wenz S., Liermann H-P., Roeh J.T., Ehnes A., Dubrovinskaia N. and Dubrovinsky L. (2019) Single-crystal diffractometer coupled with double-sided laser heating system at the Extreme Conditions Beamline P02.2 at PETRAIII. *Review of Scientific Instruments*, **90**, 73907, doi: 10.1063/1.5108881

Černý P. (1991a) Rare-element granitic pegmatites. Part I: Anatomy and internal evolution of pegmatite deposits. *Geoscience Canada*, **18**, 49–67

Černý P. (1991b) Rare-element granitic pegmatites. Part II: Regional to global environments and petrogenesis. *Geoscience Canada*, **18**, 68–81

Černý P. and Ercit T.S. (2005) The classification of granitic pegmatites revisited. *The Canadian Mineralogist*, **43**, 2005–2026, doi: 10.2113/gscanmin.43.6.2005

Chervin J.C., Canny B. and Mancinelli M. (2001) Ruby-spheres as pressure gauge for optically transparent high pressure cells. *High Pressure Research*, **21**, 305–314, doi: 10.1080/08957950108202589

Clavier N., Podor R. and Dacheux N. (2011) Crystal chemistry of the monazite structure. *Journal of the European Ceramic Society*, **31**, 941–976, doi: 10.1016/j.jeurceramsoc.2010.12.019

Crichton W.A., Parise J.B., Antao S.M. and Grzechnik A. (2005) Evidence for monazite-, barite-, and $AgMnO_4$ (distorted barite)-type structures of $CaSO_4$ at high pressure and temperature. *American Mineralogist*, **90**, 22–27, doi: 10.2138/am.2005.1654.

Crichton W.A., Merlini M., Müller H., Chantel J. and Hanfland M. (2012) The high-pressure monazite-to-scheelite transformation in $CaSeO_4$. *Mineralogical Magazine*, **76**, 913–923. doi: 10.1180/minmag.2012.076.4.08

Davis J.B., Marshall D.B., Housley R.M. and Morgan P.E.D. (1998) Machinable Ceramics Containing Rare-Earth Phosphates. *Journal of the American Ceramic Society*, **81**, 2169–2175, doi: 10.1111/j.1151–2916.1998.tb02602.x

Errandonea D., Kumar R., López-Solano J., Rodríguez-Hernández P., Muñoz A., Rabie M.G. and Sáez Puche R. (2011) Experimental and theoretical study of structural properties and phase transitions in $YAsO_4$ and $YCrO_4$. *Physical Review B*, **83**, 245, doi: 10.1103/PhysRevB.83.134109

Errandonea D. and Kumar R.S. (2014) High-pressure structural transformations of $PbCrO_4$ up to 51.2 GPa: An angle-dispersive synchrotron X-ray diffraction study. *Materials Research Bulletin*, **60**, 206–211, doi: 10.1016/j.materresbull.2014.08.041

Errandonea D., Pellicer-Porres J., Martínez-García D., Ruiz-Fuertes J., Friedrich A., Morgenroth W., Popescu C., Rodríguez-Hernández P., Muñoz A. and Bettinelli M. (2016) Phase stability of lanthanum orthovanadate at high pressure. *Journal of Physical Chemistry C*, **120**, 13749–13762, doi: 10.1021/acs.jpcc.6b04782

Errandonea D. (2017) High-pressure phase transitions and properties of MTO_4 compounds with the monazite-type structure. *Physica Status Solidi B*, **254**, 1700016, doi: 10.1002/pssb.201700016

Errandonea D., Gomis O., Rodríguez-Hernández P., Muñoz A., Ruiz-Fuertes J., Gupta M., Achary S.N., Hirsch A., Manjon F.J., Peters L., Roth G., Tyagi A.K. and Bettinelli M. (2018) High-pressure structural and vibrational properties of monazite-type $BiPO_4$, $LaPO_4$, $CePO_4$, and $PrPO_4$. *Journal of Physics: Condensed Matter*, **30**, 65401, doi: 10.1088/1361-648X/aaa20d

Finch R.J. and Hanchar J.M.(2003) Structure and chemistry of zircon and zircon-group minerals. Pp. 1–25 in: *Zircon* (John M. Hanchar and Paul W.O. Hoskin, editors). Reviews in Mineralogy and Geochemistry, **53**. The Mineralogical Society of America and the Geochemical Society, Chantilly, Virginia, USA, doi: 10.2113/0530001

Fukunaga O. and Yamaoka S. (1979) Phase transformations in ABO_4 type compounds under high pressure. *Physics and Chemistry of Minerals*, **5**, 167–177, doi: 10.1007/BF00307551

Gleissner J., Errandonea D., Segura A., Pellicer-Porres J., Hakeem M.A., Proctor J.E., Raju S.V., Kumar R.S., Rodríguez-Hernández P., Muñoz A., Lopez-Moreno S. and Bettinelli M. (2016) Monazite-type $SrCrO_4$ under compression. *Physical Review B*, **94**, 134108, doi: 10.1103/PhysRevB.94.134108

Gonzalez-Platas J., Alvaro M., Nestola F. and Angel R.J. (2016) EosFit7-GUI: a new graphical user interface for equation of state calculations, analyses and teaching. *Journal of Applied Crystallography*, **49**, 1377–1382, doi: 10.1107/S1600576716008050.

Graeser S. and Albertini C. (1995) Wannigletscher und Conca Cervandone. *Lapis*, **20**, 41–64.

Guastoni A., Pezzotta F. and Vignola P. (2006) Characterization and genetic inferences of arsenates, sulfates and vanadates of Fe, Cu, Pb, Zn from Mount Cervandone (Western Alps, Italy). *Periodico di Mineralogia*, **75**, 141–150.

Harrison T.M., Catlos E.J. and Montel J-M. (2002) U-Th-Pb dating of phosphate minerals. Pp. 524–558 in: *Micas: Crystal Chemistry & Metamorphic Petrology* (Annibale Mottana, Francesco Paolo Sassi, James B. Thompson, Jr. and Stephen Guggenheim, editors). Reviews in Mineralogy and Geochemistry, 48. The Mineralogical Society of America and the Geochemical Society, Chantilly, Virginia, USA, doi: 10.2138/rmg.2002.48.14.

Hassel O. (1926) XIV. Die Kristallstruktur einiger Verbindungen von der Zusammensetzung MRO_4. I. Zirkon $ZrSiO_4$. *Zeitschrift für Kristallographie – Crystalline Materials*, **63**, 247–254, doi: 10.1524/zkri.1926.63.1.247

Hay R.S., Mogilevsky P. and Boakye E. (2013) Phase transformations in xenotime rare-earth orthophosphates. *Acta Materialia*, **61**, 6933–6947, doi: 10.1016/j.actamat.2013.08.005

Heuser J.M., Palomares R.I., Bauer J.D., Rodriguez M.L., Cooper J., Lang M., Scheinost A.C., Schlenz H., Winkler B., Bosbach D., Neumeier S. and Deissmann G. (2018) Structural characterization of $(Sm,Tb)PO_4$ solid solutions and pressure-induced phase transitions. *Journal of the European Ceramic Society*, **38**, 4070–4081, doi: 10.1016/j.jeurceramsoc.2018.04.030

Holland T.J.B. and Powell R. (1998) An internally consistent thermodynamic data set for phases of petrological interest. *Journal Metamorphic Geology*, **16**, 309–343, doi: 10.1111/j.1525-1314.1998.00140.x

Huang T., Lee J-S., Kung J. and Lin C-M. (2010) Study of monazite under high pressure. *Solid State Communications*, **150**, 1845–1850, doi: 10.1016/j.ssc.2010.06.042

Jayaraman A., Kourouklis G.A., Espinosa G.P., Cooper A.S. and van Uitert L.G. (1987) A high-pressure Raman study of yttrium vanadate (YVO_4) and the pressure-induced transition from the zircon-type to the scheelite-type structure. *Journal of Physics and Chemistry of Solids*, **48**, 755–759, doi: 10.1016/0022-3697(87)90072-2

Kahle H.G., Schopper H.C., Urban W. and Wüchner W. (1970) Temperature effects on zircon structure lattice parameters and zero-field resonance for substituted Gd^{3+}. *Physica Status Solidi B*, **38**, 815–819, doi: 10.1002/pssb.19700380231

Klotz S., Chervin J-C., Munsch P. and Le Marchand G. (2009) Hydrostatic limits of 11 pressure transmitting media. *Journal of Physics D*, **42**, 075413, http://dx.doi.org/10.1088/0022-3727/42/7/075413

Kolitsch U. and Holtstam D. (2004) Crystal chemistry of $REEXO_4$ compounds (X = P,As,V). II. Review of $REEXO_4$ compounds and their stability fields. *European Journal of Mineralogy*, **16**, 117–126, doi: 10.1127/0935-1221/2004/0016-0117

Krüger H. and Breil L. (2009) Computer-controlled high-temperature single-crystal X-ray diffraction experiments and temperature calibration. *Journal of Applied Crystallography*, **42**, 140–142, doi: 10.1107/S0021889808035607

Lacomba-Perales R., Errandonea D., Meng Y. and Bettinelli M. (2010) High-pressure stability and compressibility of APO_4 (A=La, Nd, Eu, Gd, Er, and Y) orthophosphates: An X-ray diffraction study using synchrotron radiation. *Physical Review B*, **81**, 21, doi: 10.1103/PhysRevB.81.064113

Langreiter T. and Kahlenberg V. (2015) TEV—A program for the determination of the thermal expansion tensor from diffraction data. *Crystals*, **5**, 143–153, doi: 10.3390/cryst5010143

Lausi A., Polentarutti M., Onesti S., Plaisier J.R., Busetto E., Bais G., Barba L., Cassetta A., Campi G., Lamba D., Pifferi A., Mande S.C., Sarma D.D., Sharma S.M. and Paolucci G. (2015) Status of the crystallography beamlines at Elettra. *European Physical Journal Plus*, **130**, 2476, doi: 10.1140/epjp/i2015-15043-3

Li H., Zhang S., Zhou S. and Cao X. (2009) Bonding characteristics, thermal expansibility, and compressibility of RXO(4) (R = rare earths, X = P, As) within monazite and zircon structures. *Inorganic Chemistry*, **48**, 4542–4548, doi: 10.1021/ic900337j

Liermann H-P. *et al.* (2015) The Extreme Conditions Beamline P02.2 and the Extreme Conditions Science Infrastructure at PETRA III. *Journal of Synchrotron Radiation*, **22**, 908–24, doi: 10.1107/s1600577515005937.

López-Solano J., Rodríguez-Hernández P., Muñoz A., Gomis O., Santamaría-Perez D., Errandonea D., Manjón F.J., Kumar R.S., Stavrou E. and Raptis C. (2010) Theoretical and experimental study of the structural stability of $TbPO_4$ at high pressures. *Physical Review B*, 81:21, doi: 10.1103/PhysRevB.81.144126

Manjón F.J., Rodríguez-Hernández P., Muñoz A., Romero A.H., Errandonea D., Syassen K. (2010) Lattice dynamics of YVO_4 at high pressures. *Physical Review B*, **81**, 90. doi: 10.1103/PhysRevB.81.075202

Mao H.K., Xu J., Bell P.M. (1986) Calibration of the ruby pressure gauge to 800 kbar under quasi-hydrostatic conditions. *Journal of Geophysical Research*, **91**, 4673–4676, doi: 10.1029/JB091iB05p04673

Marqueño T., Errandonea D., Pellicer-Porres J., Santamaria-Perez D., Martinez-Garcia D., Bandiello E., Rodriguez-Hernandez P., Muñoz A., Achary S.N., Popescu C. (2021) Polymorphism of praseodymium orthovanadate under high pressure. *Physical Review B*, **103**, doi: 10.1103/PhysRevB.103.134113

Merlini M. and Hanfland M. (2013) Single-crystal diffraction at megabar conditions by synchrotron radiation. High Pressure Research 33:511–522. doi: 10.1080/08957959.2013.831088

Momma K. and Izumi F. (2011) VESTA 3 for three-dimensional visualization of crystal, volumetric and morphology data. *Journal of Applied Crystallography*, **44**, 1272–1276, doi: 10.1107/S0021889811038970

Mooney R.C.L. (1948) Crystal structures of a series of rare earth phosphates. *The Journal of Chemical Physics*, **16**, 1003, doi: 10.1063/1.1746668

Morgan P.E.D., Marshall D.B. and Housley R.M. (1995) High-temperature stability of monazite-alumina composites. *Materials Science and Engineering: A*, **195**, 215–222, doi: 10.1016/0921-5093(94)06521-7

Mullica D.F., Milligan W.O., Grossie D.A., Beall G.W. and Boatner L.A. (1984) Ninefold coordination LaPO4: Pentagonal interpenetrating tetrahedral polyhedron. *Inorganica Chimica Acta*, **95**, 231–236, doi: 10.1016/S0020-1693(00)87472-1

Musselman M.A. (2017) In situ Raman spectroscopy of pressure-induced phase transformations in $DyPO_4$ and $Gd_xD_{y(1-x)}PO_4$. MSc thesis, Colorado School of Mines, USA.

Ni Y., Hughes J.M., Mariano A.N. (1995) Crystal chemistry of the monazite and xenotime structures. *American Mineralogist*, **80**, 21–26, doi: 10.2138/am-1995-1-203

Oelkers E.H. and Montel J-M. (2008) Phosphates and nuclear waste storage. *Elements*, **4**, 113–116, doi: 10.2113/GSELEMENTS.4.2.113

Orlova A.I. and Ojovan M.I. (2019) Ceramic mineral waste-forms for nuclear waste immobilization. *Materials (Basel)*, **12**, doi: 10.3390/ma12162638

Pagliaro F., Lotti P., Comboni D., Battiston T., Guastoni A., Fumagalli P., Rotiroti N. and Gatta G.D. (2022a) High-pressure behaviour of gasparite-(Ce) (nominally $CeAsO_4$), a monazite-type arsenate. *Physics and Chemistry of Minerals*, **49**, 569, doi: 10.1007/s00269-022-01222-5

Pagliaro F., Lotti P., Guastoni A., Rotiroti N., Battiston T. and Gatta G.D. (2022b) Crystal chemistry and miscibility of chernovite-(Y), xenotime-(Y), gasparite-(Ce) and monazite-(Ce) from Mt. Cervandone, Western Alps, Italy. *Mineralogical Magazine*, **86**, 150–167, doi: 10.1180/mgm.2022.5

Panchal V., Errandonea D., Manjón F.J., Muñoz A., Rodríguez-Hernández P., Achary S.N. and Tyagi A.K. (2017) High-pressure lattice-dynamics of $NdVO_4$. *Journal of Physics and Chemistry of Solids*, **100**, 126–133, doi: 10.1016/j.jpcs.2016.10.001

Parrish W. (1939) Unit cell and space group of monazite, $(La,Ce,Y)PO_4$. *American Mineralogist*, **24**, 651–652.

Pawley A.R., Redfern S.A.T. and Holland T.J.B. (1996) Volume behaviour of hydrous minerals at high pressure and temperature; I, Thermal expansion of lawsonite, zoisite, clinozoisite, and diaspore. *American Mineralogist*, **81**, 335–340, doi: 10.2138/am-1996-3-407

Perrière L., Bregiroux D., Naitali B., Audubert F., Champion E., Smith D.S. and Bernache-Assollant D. (2007) Microstructural dependence of the thermal and mechanical properties of monazite $LnPO_4$ (Ln=La to Gd). *Journal of the European Ceramic Society*, **27**, 3207–3213, doi: 10.1016/j.jeurceramsoc.2006.12.005

Petříček V., Palatinus L., Plášil J. and Dušek M. (2023) JANA2020 – a new version of the crystallographic computing system JANA. *Zeitschrift für Kristallographie – Crystalline Materials*, **238**, 271–282. doi: 10.1515/zkri-2023-0005

Poreba T., Comboni D. and Mezouar M., *et al* (2022) Tracking of structural phase transitions via single crystal x-ray diffraction at extreme conditions: advantages of extremely brilliant source. *Journal of Physics: Condensed Matter*, **35**, doi: 10.1088/1361-648X/aca50b

Prescher C. and Prakapenka V.B. (2015) DIOPTAS: a program for reduction of two-dimensional X-ray diffraction data and data exploration. *High Pressure Research*, **35**, 223–230, doi: 10.1080/08957959.2015.1059835

Rapp R.P. and Watson E.B. (1986) Monazite solubility and dissolution kinetics: implications for the thorium and light rare earth chemistry of felsic magmas. *Contributions to Mineralogy and Petrology*, **94**, 304–316, doi: 10.1007/BF00371439

Rebuffi L., Plaisier J.R., Abdellatief M., Lausi A. and Scardi P. (2014) MCX: a synchrotron radiation beamline for X-ray diffraction line profile analysis. *Zeitschrift für anorganische und allgemeine Chemie*, **640**, 3100–3106. doi: 10.1002/zaac.201400163

Reddy C.V.V., Satyanarayana Murthy K. and Kistaiah P. (1988) X-ray study of the thermal expansion anisotropy in YVO_4 and $YAsO_4$ compounds. *Solid State Communications*, **67**, 545–547. doi: 10.1016/0038-1098(84)90179-0

Rigaku Oxford Diffraction (2020) *CrysAlisPro version 171.41.93*. Wroclaw, Poland

Rothkirch A., Gatta G.D., Meyer M., Merkel S., Merlini M. and Liermann H.P. (2013) Single-crystal diffraction at the Extreme Conditions beamline P02.2: procedure for collecting and analyzing high-pressure single-crystal data. *Journal of Synchrotron Radiation*, 20, 711–720. doi: 10.1107/S0909049513018621

Ruiz-Fuertes J., Hirsch A., Friedrich A., Winkler B., Bayarjargal L., Morgenroth W., Peters L., Roth G. and Milman V. (2016) High-pressure phase of $LaPO_4$ studied by X-ray diffraction and second harmonic generation. *Physical Review B*, **94**, 203. doi: 10.1103/PhysRevB.94.134109

Schopper H.C., Urban W. and Ebel H. (1972) Measurements of the temperature dependence of the lattice parameters of some rare earth compounds with zircon structure. *Solid State Communications*, **11**, 955–958, doi: 10.1016/0038-1098(72)90297-9

Sousa Filho P.C. de and Serra O.A. (2009) Red, green, and blue lanthanum phosphate phosphors obtained via surfactant-controlled hydrothermal synthesis. *Journal of Luminescence*, **129**, 1664–1668, doi: 10.1016/j.jlumin.2009.04.075

Stangarone C., Angel R.J., Prencipe M., Mihailova B. and Alvaro M. (2019) New insights into the zircon-reidite phase transition. *American Mineralogist*, **104**, 830–837.

Stoe and Cie (2008) *WinXpose 1.7.6*. Darmstadt, Germany.

Strada M. and Schwendimann G. (1934) La struttura cristallina di alcuni fosfati ed arseniati di metalli trivalenti. II. Arseniato e fosfato di yttrio. *Gazzetta Chimica Italiana*, **1934**, 662–674.

Strzelecki A.C., Zhao X., Estevenon P., Xu H., Dacheux N., Ewing R.C. and Guo X. (2024) Crystal chemistry and thermodynamic properties of zircon structure-type materials. *American Mineralogist*, **109**, 225–242, doi: 10.2138/am-2022-8632

Subbarao E.C., Agrawal D.K., McKinstry H.A., Sallese C.W. and Roy R. (1990) Thermal Expansion of Compounds of Zircon Structure. *Journal of the American Ceramic Society*, **73**, 1246–1252, doi: 10.1111/j.1151-2916.1990.tb05187.x

Tatsi A., Stavrou E., Boulmetis Y.C., Kontos A.G., Raptis Y.S. and Raptis C. (2008) Raman study of tetragonal $TbPO_4$ and observation of a first-order phase transition at high pressure. *Journal of Physics: Condensed Matter*, **20**, 425216, doi: 10.1088/0953-8984/20/42/425216

Toby B.H. and von Dreele R.B. (2013) GSAS-II: the genesis of a modern open-source all purpose crystallography software package. *Journal of Applied Crystallography*, **46**, 544–549, doi: 10.1107/S0021889813003531

Ueda T. (1953) The crystal structure of monazite ($CePO_4$). *Memoirs of the College of Science*, University of Kyoto, Series B, **1953**, 227–246.

Ueda T. (1967) Reexamination of the crystal structure of monazite. *The Journal of the Japanese Association of Mineralogists, Petrologists and Economic Geologists*, **58**, 170–179, doi: 10.2465/ganko1941.58.170

Ushakov S.V., Helean K.B., Navrotsky A. and Boatner L.A. (2001) Thermochemistry of rare-earth orthophosphates. *Journal of Materials Research*, **16**, 2623–2633, doi: 10.1557/JMR.2001.0361

Vegard L. (1916) VI. Results of crystal analysis. *The London, Edinburgh, and Dublin Philosophical Magazine and Journal of Science*, **32**, 65–96, doi: 10.1080/14786441608635544

Vegard L. (1926) CIV. Results of crystal analysis. *The London, Edinburgh, and Dublin Philosophical Magazine and Journal of Science*, **1**, 1151–1193, doi: 10.1080/14786442608633716

Vegard L. (1927) XLVII. The structure of xenotime and the relation between chemical constitution and crystal structure. *The London, Edinburgh, and Dublin Philosophical Magazine and Journal of Science*, **4**, 511–525, doi: 10.1080/14786440908564357

Vorres K.S. (1962) Correlating ABO_4 compound structures. *Journal of Chemical Education*, **39**, 566, doi: 10.1021/ed039p566

Wang X., Loa I., Syassen K., Hanfland M. and Ferrand B. (2004) Structural properties of the zircon- and scheelite-type phases of YVO_4 at high pressure. *Physical Review B*, 70, 449, doi: 10.1103/PhysRevB.70.064109

Wyckoff R.W.G. and Hendricks S.B. (1928) IV. Die Kristallstruktur von Zirkon und die Kriterien für spezielle Lagen in tetragonalen Raumgruppen. *Zeitschrift für Kristallographie - Crystalline Materials*, **66**, 73–102, doi: 10.1524/zkri.1928.66.1.73

Yuan H., Wang K., Wang C., Zhou B., Yang K., Liu J. and Zou B. (2015) Pressure-Induced Phase Transformations of Zircon-Type $LaVO_4$ Nanorods. *Journal of Physical Chemistry C*, **119**, 8364–8372, doi: 10.1021/acs.jpcc.5b01007

Zhang S., Zhou S., Li H. and Li L. (2008) Investigation of thermal expansion and compressibility of rare-earth orthovanadates using a dielectric chemical bond method. *Inorganic Chemistry*, **47**, 7863–7867, doi: 10.1021/ic800672h

Zhang F.X., Wang J.W., Lang M., Zhang J.M., Ewing R.C. and Boatner L.A. (2009) High-pressure phase transitions of ScPO4 and YPO4. *Physical Review B*, **80**, 18411, doi: 10.1103/PhysRevB.80.184114